ļ

Downloaded from https://academic.oup.com/mnras/article/530/2/1563/7641412 by University of Colorado user on 12 September 2024

MNRAS **530**, 1563–1579 (2024) Advance Access publication 2024 April 05

The relationship between simulated sub-millimeter and near-infrared images of Sagittarius A* from a magnetically arrested black hole accretion flow

A. A. Grigorian ¹⁰1,2★ and J. Dexter ¹⁰1,3★

Accepted 2024 March 28. Received 2024 March 28; in original form 2023 November 11

ABSTRACT

Sagittarius A* (Sgr A*), the supermassive black hole at the centre of the Milky Way, undergoes large-amplitude near-infrared (NIR) flares that can coincide with the continuous rotation of the NIR emission region. One promising explanation for this observed NIR behaviour is a magnetic flux eruption, which occurs in three-dimensional General Relativistic Magneto-Hydrodynamic (3D GRMHD) simulations of magnetically arrested accretion flows. After running two-temperature 3D GRMHD simulations, where the electron temperature is evolved self-consistently along with the gas temperature, it is possible to calculate ray-traced images of the synchotron emission from thermal electrons in the accretion flow. Changes in the gas-dominated ($\sigma = b^2/2\rho < 1$) regions of the accretion flow during a magnetic flux eruption reproduce the NIR flaring and NIR emission region rotation of Sgr A* with durations consistent with observation. In this paper, we demonstrate that these models also predict that large (1.5x – 2x) size increases of the sub-millimeter (sub-mm) and millimeter (mm) emission region follow most NIR flares by 20–50 min. These size increases occur across a wide parameter space of black hole spin (a = 0.3, 0.5, -0.5, and 0.9375) and initial tilt angle between the accretion flow and black hole spin axes θ_0 ($\theta_0 = 0^\circ$, 16° , and 30°). We also calculate the sub-mm polarization angle rotation and the shift of the sub-mm spectral index from zero to -0.8 during a prominent NIR flare in our high spin (a = 0.9375) simulation. We show that, during a magnetic flux eruption, a large ($\sim 10r_g$), magnetically dominated ($\sigma > 1$), low-density, and high-temperature 'bubble' forms in the accretion flow. The drop in density inside the bubble and additional electron heating in accretion flow between $15r_g$ and $25r_g$ leads to a sub-mm size increase in corresponding images.

Key words: accretion, accretion discs – black hole physics – gravitational lensing: strong – MHD – radiation mechanisms: thermal – radiative transfer.

1 INTRODUCTION

Sagittarius A* (Sgr A*), the object at the centre of the Milky Way, is a bright radio source (Balick & Brown 1974; Ekers et al. 1975; Lo et al. 1975) with variable near-infrared (NIR) emission reaching a factor of 10x - 25x (Genzel et al. 2003b; Ghez et al. 2004; GRAVITY Collaboration et al. 2020b) its median value in flux (Dodds-Eden et al. 2011; Schodel et al. 2011; Witzel et al. 2018). Sgr A* also exhibits X-ray flares reaching 50x the quiescent value (Markoff et al. 2001) which often coincide with an NIR flare (Baganoff et al. 2001; Genzel et al. 2003a; Ghez et al. 2004; Eckart et al. 2008; Ponti et al. 2017; GRAVITY Collaboration et al. 2021). Astrometry of stars orbiting Sgr A* (Genzel et al. 1997; Ghez et al. 2008) and the resolved black hole shadow at 230 GHz captured by the Event Horizon Collaboration (EHT) (Event Horizon Telescope Collaboration et al. 2022a) provide consistent and strong evidence

that Sgr A* is a supermassive black hole with mass $\sim 4 \times 10^6 \odot$. Linear polarization fractions of $\cong 10$ –40 per cent in the NIR and 230 GHz indicate that the emission region around the black hole is dominated by synchrotron radiation (Trippe et al. 2007; Eckart et al. 2008; Wielgus et al. 2022). The lack of sub-mm/mm variability on the same order as the NIR variability suggests that the origin of the flares are electrons accelerated to extreme velocities ($\gamma \gtrsim 10^3$) (Markoff et al. 2001; Dodds-Eden et al. 2009). For example, the magnetic Rayleigh–Taylor instability stemming from the interface of a dense plasma and a magnetic cavity can drive efficient particle acceleration (Zhdankin, Ripperda & Philippov 2023). Weaker flares may be also be caused by the lensing of turbulent accretion flow (Chan et al. 2015). However, the origin of the NIR flares, especially stronger ones, remains unclear.

Recently, the GRAVITY Collaboration measured the movement of SgrA*'s NIR centroid. During three NIR flares (GRAVITY Collaboration et al. 2020b), the NIR centroid made a clockwise, quasi-circular loop on the sky with a diameter of $\sim 110-140~\mu as$ over periods ranging between 40 and 70 min. Simultaneous measurements of the NIR polarization angle showed continuous rotation – a

¹ JILA, University of Colorado and National Institute of Standards and Technology, 440 UCB, Boulder, CO 80309-0440, USA

²Department of Physics, University of Colorado, Boulder, 390 UCB, Boulder, CO 80309-0390, USA

³Department of Astrophysical and Planetary Sciences, University of Colorado, Boulder, 391 UCB, Boulder, CO 80309-0391, USA

^{*}E-mail: arpi.grigorian@colorado.edu (AAG); jason.dexter@colorado.edu (JD)

1564 A. Grigorian and J. Dexter

clockwise 'loop' in Stokes \mathcal{U} , \mathcal{Q} space. The lack of a strong Doppler signal from the centroid motion constrained the inclination of the disc to be $\leq 130^{\circ}$ (GRAVITY Collaboration et al. 2020a).

Sgr A* is also known to undergo steady rotations of the submm polarization angle (Marrone et al. 2006). Using the ALMA Observatory, Wielgus et al. (2022) recently found an example of the 230-GHz polarization angle that makes a quasi-circular path in Stokes \mathcal{U} , \mathcal{Q} (similar to the path of NIR polarization angle) over a period of 74 ± 6 min following an X-ray flare.

The GRAVITY observations are well described by a hot-spot at $\simeq 6-10r_{\rm g}$ orbiting around the black hole at a low ($i \le 30^{\circ}$) inclination angle and polodial field (GRAVITY Collaboration et al. 2018; 2020b). However, these models do not address possible physical mechanisms that could change the gas and electron temperature in the inner accretion flow.

Three-dimensional General Relativistic Magneto-Hydrodynamic (GRMHD) simulations of a black hole surrounded by an accretion disc or flow offer insights into the physical mechanisms that may be present in Sgr A*. Two key GRMHD black hole accretion disc models often explored in the literature are standard and normal evolution (SANE) discs and magnetically arrested discs (MAD). SANE discs, which do not reach high levels of magnetic flux threading the horizon (Narayan et al. 2012), likely rely on the magnetorotational instability (MRI) for angular momentum transport (Hawley & Balbus 1991; Balbus & Hawley 1998). MADs, by contrast, accrete large amounts of magnetic flux that ultimately saturates (Bisnovatyi-Kogan & Ruzmaikin 1974, 1976; Igumenshchev, Narayan & Abramowicz 2003; Begelman, Scepi & Dexter 2022).

GRMHD simulations of MAD successfully reproduce many observations of Sgr A* (e.g. Ripperda, Bacchini & Philippov 2020; Dexter et al. 2020a; Chashkina, Bromberg & Levinson 2021; Collaboration 2022). MAD simulations of thick discs with high (a = 0.9375) black hole spin produce high-temperature orbiting hotspots roughly consistent with the quasi-circular motion of the NIR centroid observed by GRAVITY (Dexter et al. 2020b; Ripperda et al. 2022).

In this paper, we study similar MAD simulations as Dexter et al. (2020b) over a wider parameter space. Specifically, we vary the black hole spin a and consider simulations that begin with an initial tilt angle θ_0 between the black hole spin axis and the accretion flow spin axis. In Section 2 (Methods), we describe the GRMHD set-up, how images are created using outputted data from our simulations, and how we extract key observables from those images. Then, we focus on an example from the high spin (a = 0.9375), prograde ($\theta_0 = 0^{\circ}$) simulation where the dissipation of magnetic flux near the horizon creates a magnetically dominated, low-density 'bubble' (hot spot) within $10r_g$ of the accretion flow. The bubble itself is a high $\sigma = b^2/2\rho$ > 1 region, where $b^2/2$ is the magnetic pressure and ρ is the fluid density. However, the bubble formation and orbit around the black hole is coincident with significant electron temperature increases in regions where the plasma parameter $\sigma < 1$. When the bubble eventually reaches larger radii (15–30 $r_{\rm g}$), the electron temperature also increases in this region. We show these changes in the $\sigma < 1$ regions of the inner accretion flow not only power an NIR flare and quasi-circular NIR centroid rotation (similar to results from Dexter et al. 2020b), but also cause a significant increase in both the sub-mm and mm emission regions about 1 h after the NIR flare peak. This example produces the rotation of the sub-mm polarization angle with a period of \sim 2 h, consistent with observations (Marrone et al. 2006; Wielgus et al. 2022). The luminosity spectrum evolves during the course of the NIR flare, and the peak of the sub-mm size increase is simultaneous with a decrease in the synchotron spectrum peak

Table 1. A list of all simulations in this paper sorted by spin a and initial accretion flow tilt angle θ_0 . We ignore times prior to t_i to allow each simulation to evolve from its initial configuration and reach an MAD state. The time $t_{\rm f}$ is the duration of each simulation. We often refer to the high spin (a=0.9375), prograde simulation as the fiducial simulation in this work.

a	θ_0	t_i (GM/c ³)	$t_{\rm f}~({\rm GM/c^3})$
0.9375 (high-spin)	0° (prograde)	10 000	96 310
0.5 (low-spin)	0° (prograde)	24 000	44 390
0.9375 (high-spin)	16°	10 000	26,660
0.5 (low-spin)	16°	24 000	51710
0.3 (low-spin)	16°	26 000	48 190
0.5 (low-spin)	30°	10 000	29 190
-0.5 (low-spin)	180° (retrograde)	16 000	34 670

frequency ν_c and, as a result, a decrease in the spectral index near 230 GHz (1.3 mm).

In Section 7.1, we demonstrate that the relationship between NIR flares and the sub-mm/mm size increases is a feature of all simulations in our parameters space. The relationship between the NIR total flux and the sub-mm/mm size increases is stronger and more consistent that the relationship between the NIR total flux and the sub-mm total flux increases. We also present the NIR centroid behaviour during our simulations. Finally, we discuss limitations of the GRMHD model, the dependence of size increases on inclination angle, and the implications our results have on illuminating the physical mechanisms behind NIR flares in Sgr A*.

2 METHODS

2.1 The GRMHD MAD model

We carried out 3D GRMHD simulations for a range of black hole spin a and initial tilt angle of the accretion flow θ_0 (see Table 1 for the full parameter space). The dimensionless black hole spin is defined as $a \equiv J/(GM^2/c)$, where J is the angular momentum and M is the black hole mass. We refer to simulations with |a| > 0.5 as high-spin; simulations with $|a| \le 0.5$ are low-spin. The angle θ_0 is measured between the spin axis of the black hole and the initial angular momentum vector of the accretion flow. Simulations with $\theta_0 = 0^\circ$ are prograde (the black hole spin and the accretion flow spin are aligned). We use the convention of negative spin values for simulations where the black hole spin and the accretion flow spin are completely antialigned

Simulations were carried out using the public harmpi code (Tchekhovskoy 2019), a 3D version of HARM (Gammie, McKinney & Tóth 2003; Noble et al. 2006). All simulations studied here were initialized from a hydrodynamic equilibrium torus with an inner radius of $12r_{\rm g}$ and a pressure maximum at $25r_{\rm g}$. The (arbitrary) initial magnetic field was composed of a single poloidal loop so that $\max(p_{\rm g})/\max(p_{\rm B})=100$, where $p_{\rm g}, p_{\rm B}$ are the gas and magnetic pressures, respectively (see Tchekhovskoy, Narayan & McKinney 2011). In order to study MAD conditions, the initial magnetic field was concentrated further out in the torus so that magnetic flux could accumulate and saturate on the black hole. For more details, see Dexter et al. (2020b).

We use Kerr–Schild coordinates and a grid resolution of $320 \times 256 \times 160$ in the r, θ , and ϕ directions, respectively. The r values are spaced lognormally to resolve the important physics occurring near the horizon. The θ coordinate is irregular, chosen to concentrate resolution near the mid-plane at small radius. The metric in all simulations is fixed as the stationary Kerr metric determined

by the black hole mass and spin. We used a temporal cadence of $10\,\mathrm{GM/c^3}$ when plotting the fluid variables and observables calculated from ray-traced images as functions of time.

We also include a scheme in our simulations that self-consistently evolves the electron internal energy density for four different electron heating prescriptions along with a single, MHD fluid (Ressler et al. 2015). For this work, we choose the electron energy density calculated from the heating prescription developed by Werner et al. (2018) from their study of particle acceleration from magnetic reconnection using 2D particle-in-cell (PIC) simulations (W18). They found an empirical relationship between the electron heating fraction q_e and the ion magnetization $\sigma_i \equiv B^2/4\pi n_i m_i c^2$, where B is the upstream magnetic field, and n_i is the ion density upstream of the reconnection region (see their equation 3). The electron heating fraction ranges from 1/4 for low magnetization to 1/2 for high magnetization. W18 was able to reproduce a variety of observed signatures for Sgr A* in previous studies (Dexter et al. 2020a, 2020b). By applying W18 throughout the entire coordinate space of the simulation, our model assumes that 100 per cent of the dissipated heat is from reconnection.

We evolve our simulations out to times ranging from 20 000 to 100 000 GM/c³ (see Table 1 for the exact duration for each simulation in our parameter space). The durations are long enough for the fluid in inner ($<50r_g$) region to reach equilibrium. For all the a = 0.9375 simulations and the a = 0.5 simulation with $\theta_0 =$ 30°, we ignored the first 10 000 GM/c³ to allow the simulation to evolve from the initial configuration of the fluid to a steady state. However, the remaining low spin $a \le 0.5$ simulations took longer than 10 000 GM/c³ to start exhibiting consistent magnetic flux eruptions. Our goal is to compare simulations when they are clearly in an MAD state. Therefore, the initial period of time that we ignored for these simulations was longer and ranged from 16000 to 26000 GM/c³ (see Table 1). However, because the simulation durations were long enough, for each simulation, there was a significant ($>16\,000\,\text{GM/c}^3$) continuous period time containing magnetic flux eruptions that we could compare across our parameter space.

2.2 Synthetic black hole images

We created monochromatic images for each simulation in Table 1 using the ray-tracing radiative transfer code grtrans (Dexter, Agol & Fragile 2009; Dexter 2016). The code calculates all four Stokes parameters for each image: total intensity \mathcal{I} , linear polarization \mathcal{Q} and \mathcal{U} , and circular polarization \mathcal{V} . The grtrans code includes all relativistic effects in a Kerr space time.

We calculate the synchrotron emission with grtrans assuming a thermal distribution of electrons. We do not include emission from non-thermal electrons (see the Discussion for how non-thermal electrons may effect the sub-mm, mm, and NIR emission.) We set the inclination angle i, the angle between the black hole spin axis and the line of sight, to $i=25^\circ$ (unless otherwise noted). Since the angular momentum of the black hole is along positive z (spinning counter-clockwise) in our simulation convention, $i<90^\circ$ means that the black hole, and, generally, the accretion flow, are spinning counter clockwise on the sky.

When calculating images, we omit regions of the accretion flow which have a σ value greater than σ -cut. Unless specified otherwise, we used σ -cut = 1. For our fiducial example, we also produced images with σ -cut = 10 (see Section 8.1 in the Discussion).

We made images at 3.5 mm (86 GHz), 1.3 mm (230 GHz), and 2.2μ m (136 THz) for all simulations in this work. We refer to all 3.5-mm images as mm (millimeter), 1.3-mm images as sub-millimeter (sub-mm), and $2.2-\mu$ m images as NIR. Most images in this study use

the following fields of view as a function of frequency: $150^2~\mu as^2$ for the NIR (2.2 μm) images, $300^2~\mu as^2$ for the sub-mm (1.3 mm) images, and $400^2~\mu as^2$ for the mm (3.5 mm) images. The black hole is always centred in the field of view. With the exception of images used to calculate the luminosity spectrum, images are 300×300 pixels in size.

In order to report distances in terms of subtended angles on the sky (μ as) and times in units of minutes/hours/days, we use 8 kpc for the distance to the Galactic Centre and $M=4\times10^6~{\rm M}_{\odot}$ for the mass of the black hole. For reference, $1000~{\rm GM/c^3}$ is approximately 5.6 h.

In GRMHD simulations, the mass accretion rate across the horizon is calculated self-consistently. However, in MAD simulations, matter is accreted in clumps and this 'true' mass accretion rate is noisy. Instead of using the 'true' mass accretion rate to scale our images, we choose a constant value for the mass accretion rate mdot every 500 frames so that the average sub-mm total flux is near the observed value of \sim 3 Jy for Sgr A*. When calculating images at higher σ -cut = 10, we use a different value of mdot so that the sub-mm images for each σ -cut meet this observational total flux constraint.

The only exception to the rule above for scaling images is set of σ -cut = 1 NIR images from the high-spin, prograde simulation between 10 000 and 57 190 GM/c³. For this case, we first found a value of mdot that recreates the observed Sgr A* sub-mm total flux for the first 500 frames and calculated all the NIR images during this period of time with the same choice of mdot. Then, we calculated a 'smoothed' curve for the mass accretion rate $\langle \dot{M} \rangle$ as a function of time by taking the actual, intrinsically noisy mass accretion rate across the black hole horizon \dot{M} and smoothing it with a Gaussian kernel. We choose a standard deviation of the Gaussian kernel that produces a $\langle \dot{M} \rangle$ which is monotonically decreasing so that any peaks in \dot{M} do not erroneously create peaks in the NIR total flux curve (we also use this procedure to scale the dimensionless magnetic flux on the black hole horizon, see Section 2.7). We then scaled the NIR images by $\langle \dot{M} \rangle^2$. The NIR images from the high-spin, prograde simulation after time 57 190 GM/c³ were calculated using the former method.

2.3 Calculating total flux, centroid, and image size

We calculate the light curves, sizes, and centroid positions directly from the artrans images.

The moment of an image $M_{p, q}$ with image coordinates x, y is defined as

$$M_{p,q} = \sum_{x} \sum_{y} x^{p} y^{q} I(x, y). \tag{1}$$

The total flux $F_{\nu}=\int I_{\nu}\cos{(\theta)}\mathrm{d}\Omega$ from a far-away source can be rewritten as

$$F_{\nu} \approx \int I_{\nu}(x, y) \, \mathrm{d}x/D \, \mathrm{d}y/D,$$
 (2)

where D is the distance to the Galactic Centre and x, y are coordinates on the sky. In this coordinate system, the black hole is centred in the image. Discretizing the integral yields

$$F_{\nu} \approx M_{0.0} (r_{\sigma}/D)^2 (X/N) (Y/N),$$
 (3)

where *X*, *Y* is the total height and width of the field of view in units of the gravitational radius $r_g = GM/c^2$ and *N* is the total number of pixels along the *x* and *y* directions.

The centroid position on the sky C(x, y) is given by

$$C(x, y) = (M_{10}/M_{00}, M_{10}/M_{00}) = (\bar{I}_x, \bar{I}_y).$$
 (4)

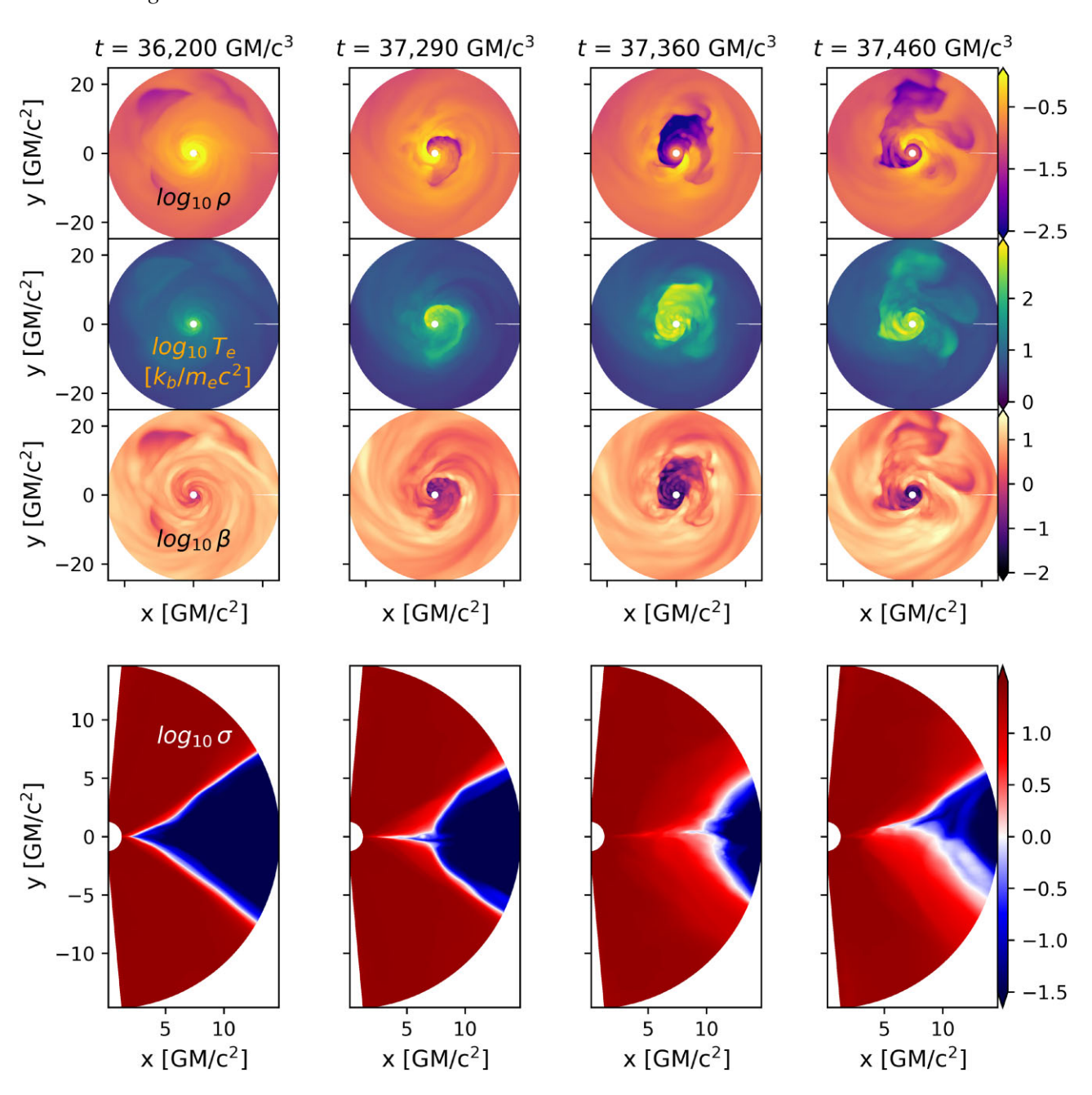


Figure 1. The density ρ (in code units), the temperature in units of kT/m_ec^2 weighted by the density ρ , and the plasma β parameter $2p/b^2$, where p is the fluid pressure and $b^2/2$ is the magnetic pressure, all averaged over polar angle θ . We also show the plasma σ parameter $b^2/2\rho$ averaged over azimuthal angle ϕ (see equations 10-13) for how we compute averages). Note that the outermost radius shown in the σ parameter plots is less than the outermost radius shown for the other fluid parameter plots. A low-density, high-temperature bubble forms in the innermost accretion flow and breaks apart before moving to larger radii during the $2000 \, \text{GM/c}^3$ interval outlined by a black box in Fig. 2. In the far left column, the accretion flow is in a quiescent state. The NIR total flux is near its median value and the sub-mm size is $\sim 50 \, \mu \text{as}$. The temperature and density is high close to the event horizon at $\sim 2r_g$ and then falls off at larger radii. Spiral structure in the density plot is visible. At $t=37\,290 \, \text{GM/c}^3$, a large scale $(10r_g)$ low-density, high-temperature, and low plasma β region forms. Also, at this time, the magnetic flux is expelled from the horizon and NIR total flux curve is at a maximum. At $t=37\,360 \, \text{GM/c}^3$, the low-density bubble has increased in size and pushed material out to larger radii. The temperature in this region stays elevated and additional smaller, even higher temperature spots appear throughout the bubble. In the rightmost column, at $t=37\,450 \, \text{GM/c}^3$, the sub-mm emission region size is at a maximum. The bubble is dissipating. The temperature in the bubble has started to cool and the density of the bubble has increased. There is a small (10x) increase in temperature in the $15-25r_g$ region. Following the trajectory of the bubble in the last three columns, one can see that it rotates counter-clockwise with the general accretion flow.

To find the size, or the spread of the intensity map, for each image, we first solve for the eigenvalues of the following matrix

$$\begin{bmatrix} M_{20}/M_{00} - (M_{10}/M_{00})^2 & M_{11}/M_{00} - (M_{10}/M_{00})(M_{01}/M_{00}) \\ M_{11}/M_{00} - (M_{10}/M_{00})(M_{01}/M_{00}) & M_{02}/M_{00} - (M_{01}/M_{00})^2 \end{bmatrix}, (5)$$

which gives the major (σ_{MAX}) and minor (σ_{MIN}) axes of an ellipse that corresponds to the 'spread' of the intensity on the image. We approximate the emission region as Gaussian and find the maximum and minimum Full-Width Half-Max $(FWHM_{MAX},$

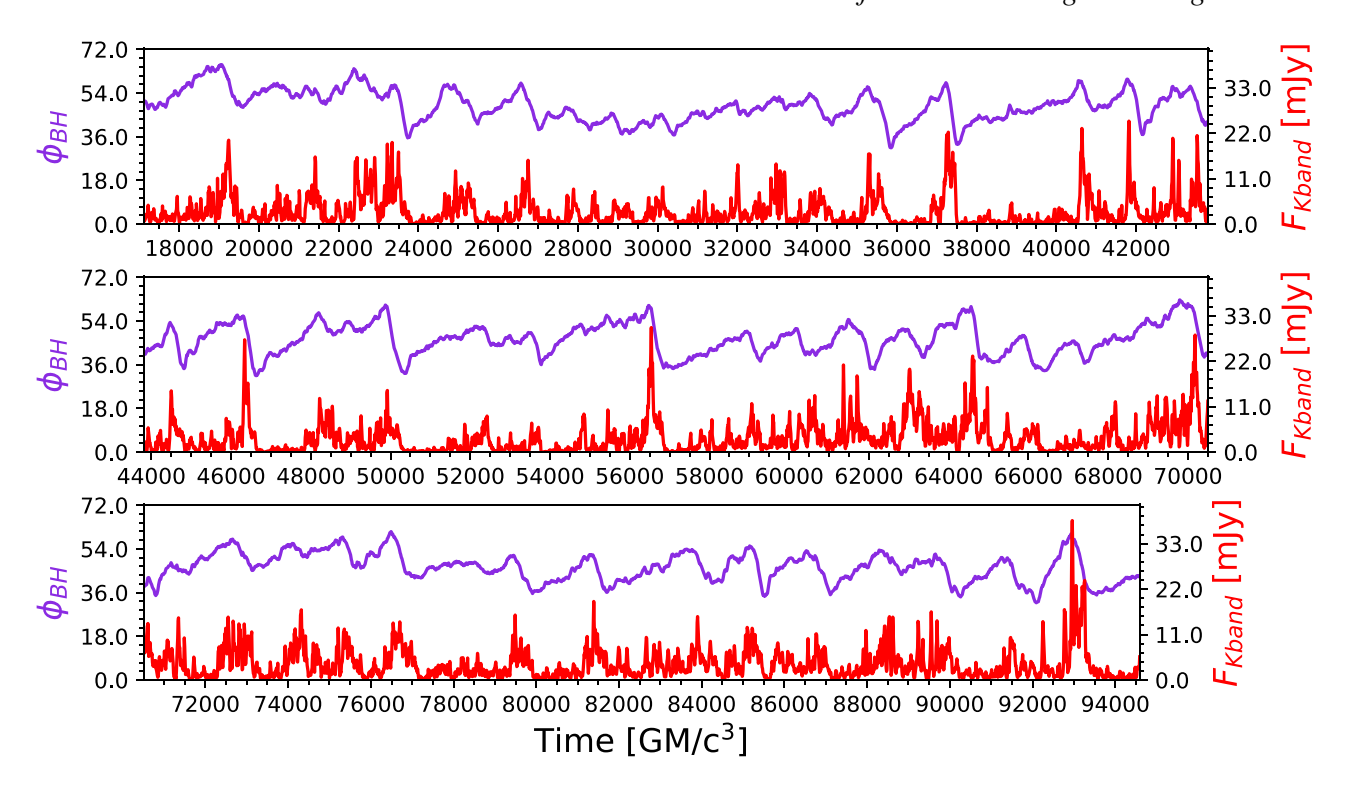


Figure 2. Dimensionless magnetic flux on the horizon ϕ_{BH} (purple) and the NIR total flux curve (red) as a function of time for the high-spin (a=0.9375) prograde simulation. The magnetic flux goes through many cycles of slow buildup followed by rapid dissipation. The dissipation of ϕ_{BH} , called a magnetic flux eruption event, coincides with a sharp peaks in the NIR total flux curve.

 $FWHM_{MIN}$, respectively) by using the simple relation

$$FWHM_{\text{MIN}} \equiv 2\sqrt{2\ln(2)}\sigma_{\text{MIN}},$$

$$FWHM_{\text{MAX}} \equiv 2\sqrt{2\ln(2)}\sigma_{\text{MAX}}.$$
 (6)

2.4 The cross-correlation coefficient

Each of the observables defined above at a single frequency, such as the total flux, \bar{I}_x , \bar{I}_y , $FWHM_{MAX}$, $FWHM_{MIN}$, produces a curve that is a discretized function of time with equal time steps: a time series. The *cross-correlation* of two time series is a convolution of one curve with the other that measures their degree of similarity as well as any characteristic lags between them.

We use the following definition of a discrete cross-correlation coefficient $\mathcal{C}\mathcal{C}$

$$\mathcal{CC}[A(t),\,B(t)](\tau) =$$

$$\frac{\sum_{i=0}^{N-\tau} (A(i) - \langle B_{0,N-\tau} \rangle) (A(i+\tau) - \langle B_{\tau,N} \rangle)}{\sqrt{\sum_{i}^{N} (A(i) - \langle A_{0,N} \rangle)^{2}} \sqrt{\sum_{i}^{N} (B(i) - \langle B_{0,N} \rangle)^{2}}}.$$
(7)

The cross-correlation $\mathcal{CC}[A(t), B(t)](\tau)$ is the functional that takes two curves A(t), B(t), and outputs a function that depends on the separation time delay τ between the two curves. The quantities $\langle A_{j,\,k} \rangle$ and $\langle B_{j,\,k} \rangle$ each correspond to the mean value to their respective functions A, B in the interval $(j,\,k)$. The maximum of $\mathcal{CC}(\tau)$ shows the strength of the correlation between two curves and the location of the peak value is a characteristic delay time τ^* .

Cross-correlation values greater than 0.5 are strong, between 0.25 and 0.5 are weak, and values less than 0.25 are practically uncorrelated.

We can use the cross-correlation function to define the autocorrelation for a single time series A(t): $\mathcal{CC}[A(t), A(t)](\tau)$. The autocorrelation function measures the periodicity of a time series; a strong autocorrelation coefficient at a non-zero τ^* suggests the curve contains a mode that has frequency $1/\tau^*$.

2.5 The structure function

The first-order structure function (SF) for a finite, continuous time series A(t) is defined as (Simonetti, Cordes & Heeschen 1985; Hughes, Aller & Aller 1992)

$$SF(\tau) = \sqrt{\frac{1}{T} \int dt \left(A(t) - A(t+\tau) \right)^2},$$
 (8)

where T is the total duration for the time series. We then find the discrete SF

$$SF(\tau_j) = \sqrt{\sum_{i=1}^{N-j} (F(t_i) - F(t_i + \tau_j))^2 / N},$$
 (9)

where N is the total number of points in our discrete time series $F(t_i)$, and apply it to our discrete time series that represent simulated observables.

The SF ignores any DC offsets present in a time series (Simonetti et al. 1985; Witzel et al. 2018; Dexter et al. 2022). Therefore, we can compare the simulated SF to observation even if there is a source of steady emission in Sgr A* or background emission that is not included in our model. For curves that are well modelled by a damped random walk, the SF reaches an asymptotic value SF_{∞} at late times (MacLeod et al. 2010). If the SF becomes close to SF_{∞} at finite time τ_{SF} , this time represents when the series becomes uncorrelated or is transitioning from red noise to white noise. We choose τ_{SF} as the time when the SF reaches its first prominent peak before plateauing.

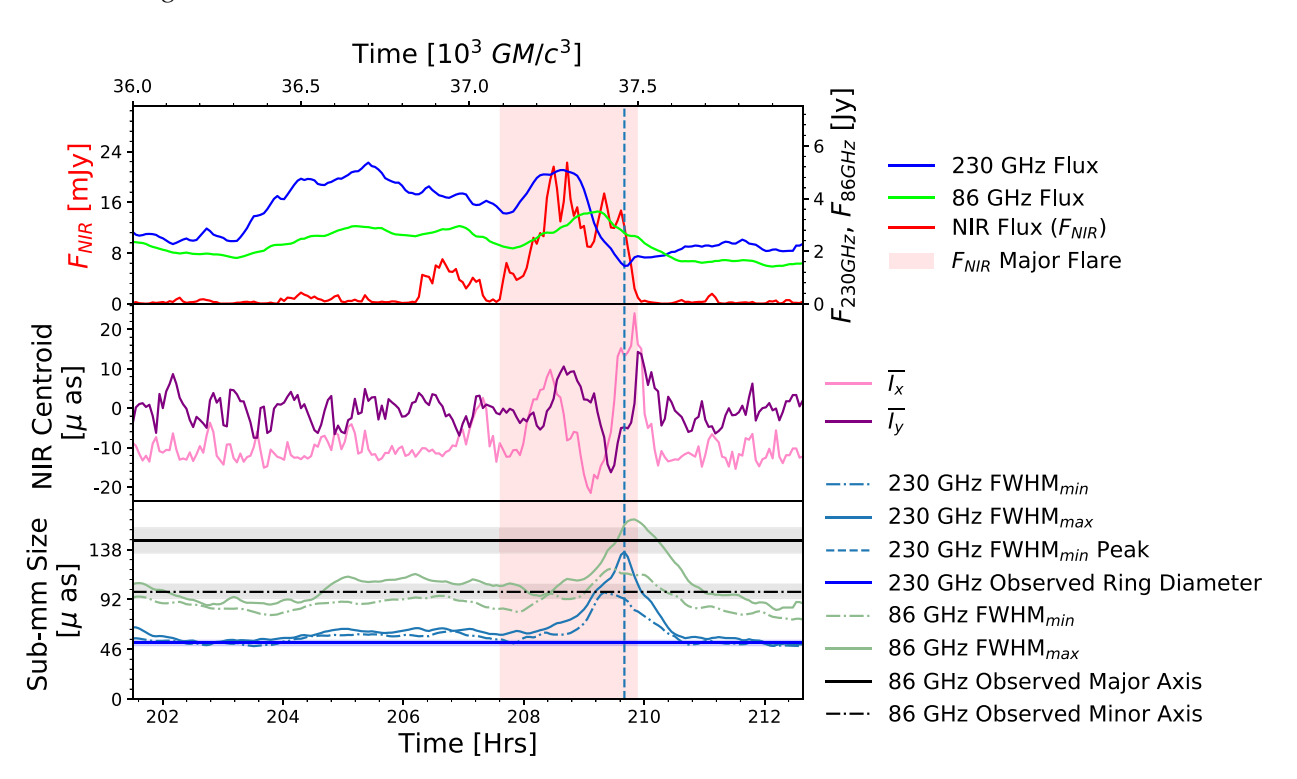


Figure 3. The evolution of key NIR, sub-mm, and mm observables before and during a prominent NIR flare. The 2000 GM/c³ interval of time shown here corresponds to the black box outlined in Fig. 2 and is taken from the high-spin, prograde simulation. In this example, the significant NIR flare results in both quasi-circular motion of the NIR centroid and an increase in the FWHM_{MAX} and FWHM_{min} of the sub-mm/mm emission region (see Section 2.3 for the definition of $FWHM_{MAX}$, $FWHM_{MIN}$ and the centroid position (\bar{I}_x , \bar{I}_y)). The light red shaded regions correspond to the second, prominent NIR flare; the dotted, vertical blue line represents the sub-mm FWHM_{MAX} peak time. Following a period of quiescence, the NIR light curve first exhibits a small, ~6 mJy flare near $36\,900\,\text{GM/c}^3$ before a second, larger (22.2 mJy) flare that reaches its peak value at $t = 37\,290\,\text{GM/c}^3$. The first flare corresponds to a minor eruption of magnetic flux, whereas the larger flare occurs during a more dramatic magnetic flux eruption event. Prior to the second flare, both the NIR centroid (middle subplot) and the sub-mm/mm size (lower subplot) undergo only small deviations from their median values. However, during the second flare, the NIR centroid changes its behaviour and makes a quasi-circular orbit around the black hole. The sub-mm and mm sizes begin to climb. The sub-mm peak size increase at 37 460 GM/c³ coincides with a final, lesser NIR total flux peak during the second flare before the total flux quickly drops to its median value. The mm FWHM_{MAX} reaches at maximum only 10 min after the sub-mm FWHM_{MAX} peak and outside the flaring period. Then, the sub-mm and mm sizes slowly decrease back to their quiescent values. The entire event, from the beginning of the first flare to the end of the sub-mm/mm size increases, lasts 800 GM/c³, or just under 4.5 h. However, the separation between the peak value of the prominent NIR flare and the sub-mm FWHM_{MAX} peak is only 57 min (270 GM/c³). The width of the sub-mm size increase peak is less than 2 h. We also include the observed sub-mm size from the EHT (Event Horizon Telescope Collaboration et al. 2022a) and the observed mm sizes from ALMA (Issaoun et al. 2021) in the bottom panel of the plot. The light blue region around the blue EHT line represents the 68 per cent credible interval; the light grey region around the observed mm $FWHM_{MAX}/FWHM_{min}$ lines represents the 95 per cent confidence interval for each measurement. We discuss the agreement between the sub-mm size and our model, as well as the tension between our calculated mm sizes and the observed values, in Section 8.6 of the Discussion.

2.6 Computing average values of fluid variables

In this work, most of our plots of fluid variables show averages of that variable over the polar angle θ or the azimuthal angle ϕ . For some function $f(r, \theta, \phi)$ that represents a scalar field of the fluid, the polar and azimuthally averaged values $\langle f(r, \phi) \rangle$ and $\langle f(r, \theta) \rangle$ are,

$$\langle f(r,\phi) \rangle = \frac{\int_{\theta=0}^{\theta=\pi} d\theta \sqrt{-g} f(r,\theta,\phi)}{\int_{\theta=0}^{\theta=\pi} d\theta \sqrt{-g}},$$
(10)

$$\langle f(r,\phi) \rangle = \frac{\int_{\theta=0}^{\theta=\pi} d\theta \sqrt{-g} f(r,\theta,\phi)}{\int_{\theta=0}^{\theta=\pi} d\theta \sqrt{-g}},$$

$$\langle f(r,\theta) \rangle = \frac{\int_{\phi=0}^{\phi=2\pi} d\phi \sqrt{-g} f(r,\theta,\phi)}{\int_{\phi=0}^{\phi=2\pi} d\phi \sqrt{-g}}.$$
(10)

Sometimes it is more instructive to show the weighted average of a fluid variable with respect to the density ρ . The weighted averages over θ and ϕ are given, respectively, as

$$\langle \tilde{f}(r,\phi) \rangle = \frac{\int_{\theta=0}^{\theta=\pi} d\theta \sqrt{-g} \rho(r,\theta,\phi) f(r,\theta,\phi)}{\int_{\theta=0}^{\theta=\pi} d\theta \sqrt{-g} \rho(r,\theta,\phi)},$$
 (12)

$$\langle \tilde{f}(r,\theta) \rangle = \frac{\int_{\phi=0}^{\phi=2\pi} d\phi \sqrt{-g} \rho(r,\theta,\phi) f(r,\theta,\phi)}{\int_{\phi=0}^{\phi=2\pi} d\phi \sqrt{-g} \rho(r,\theta,\phi)}.$$
 (13)

2.7 Calculating the dimensionless magnetic flux on the event

As the simulation evolves, magnetized material accretes on to the black hole. This process allows the magnetic flux threading the surface just outside the event horizon to accumulate. The total magnetic flux Φ at over the spherical shell at radius R is defined

$$\Phi = \sqrt{4\pi} \int_{r=R} d\theta d\phi \, B^r \sqrt{-g}, \tag{14}$$

where B^r is the radial component of the three-vector magnetic field and $\sqrt{-g}$ is the determinant of the metric.

Instead of Φ , we use the *dimensionless* magnetic flux ϕ_{BH} given by

$$\phi_{\rm BH} = \Phi_{\rm BH} / \sqrt{\langle \dot{M} \rangle}. \tag{15}$$

We calculate smoothed mass accretion rate $\langle \dot{M} \rangle$ by taking the actual, intrinsically noisy mass accretion rate across the black hole horizon \dot{M} and smoothing it with a Gaussian kernel. We set the standard deviation of the Gaussian kernel so $\langle \dot{M} \rangle$ is monotonically decreasing; this step ensures that the variability of \dot{M} does not translate to the dimensionless magnetic flux curve (this is similar to the procedure used to scale the total flux of some of our NIR images). Therefore, all the fluctuations seen in $\phi_{\rm BH}$ are due to changes in the magnetic flux rather than due to variability in the mass accretion rate.

3 MAGNETIC FLUX ERUPTIONS IN THE MAGNETICALLY ARRESTED ACCRETION FLOW

For all simulations studied, the magnetic flux on the horizon $\phi_{\rm BH}$ enter periods of slow build up followed by rapid dissipation. Most drops in $\phi_{\rm BH}$, called *magnetic flux eruptions*, are also accompanied by significant increases in the NIR total flux: an NIR flare.

Fig. 2 shows that $\phi_{\rm BH}$ cycles many times during the high-spin, prograde simulation. Most significant drops in magnetic flux are also accompanied by NIR flares. We find the average time between magnetic flux eruptions to be roughly $\sim 1600~{\rm GM/c^3}~(\sim 9~{\rm h})$, although the low (0.2) autocorrelation peak of the $\phi_{\rm BH}$ curve suggests no consistent period of recurrence for the magnetic flux eruptions.

Fig. 1 shows the evolution of several fluid variables during the course of a magnetic flux eruption taken from the high-spin, prograde simulation (all times occur within the time interval outlined by a black box in Fig. 2).

Shortly after the magnetic flux peak at $37\,230\,\mathrm{GM/c^3}$, a low-density, high-temperature 'bubble' begins to form in the accretion flow. At $37\,290\,\mathrm{GM/c^3}$, the NIR total flux curve reaches the most prominent peak during this magnetic flux eruption event. The bubble is now $\sim\!10r_\mathrm{g}$ in size and the electron temperature in the bubble is $100\mathrm{x}-1000\mathrm{x}$ the median value (second column in Fig. 1). The fluid parameter $\sigma=b^2/2\rho$ has also increased above and below the equatorial plane; only a thin region within $\sim\!7r_\mathrm{g}$ of the accretion flow remains mostly $\sigma<1$.

As the bubble rotates around the black hole, it continues to grow. By $37\,360\,\text{GM/c}^3$, the bubble is $\sim 15r_g$ in size (third column in Fig. 1). At this time, the innermost ($\lesssim 10r_g$) region of the accretion flow is mostly magnetically dominated. The sub-mm size is also increasing (see Figs 3 and 4).

Around 37 400 GM/c³, the low-density region becomes elongated; it stretches to radii $\sim 20r_{\rm g}$. Density plots of the slice along the equatorial plane show that a single, low-density region breaks apart into multiple low-density regions. By 37 460 GM/c³, the slice of the equatorial plane also shows that the low-density region within $\sim 10r_{\rm g}$ remains magnetically dominated but the σ value of the low-density region at larger radii has decreased to less than one. Also, at 37 460 GM/c³, the electron temperature has increased to 10x the median value in the $15-25r_{\rm g}$ region of the accretion flow. The temperature within $\sim 10r_{\rm g}$ remains elevated (last column of Fig. 1). The sub-mm size at 37 460 GM/c³ is at a maximum (see Fig. 4 for the sub-mm image corresponding to this time).

Throughout all the events described above, the magnetic flux has been monotonically decreasing. The magnetic flux reaches a minimum at 37 540 GM/c³. By this time, the outer region of the

bubble has reached $30r_g$. The sub-mm size is still elevated from its median value but is decreasing.

The total time between the magnetic flux peak and its local minimum is $310 \,\text{GM/c}^3$, or $1.7 \,\text{h}$.

4 NIR TOTAL FLUX AND SUB-MM/MM TOTAL FLUX AND SIZE DURING A MAGNETIC FLUX ERUPTION

During the course of our fiducial magnetic flux eruption explored above (Section 3), the NIR flux significantly increases or 'flares'. It reaches a peak value of 22.2 mJy, or 10x of the median NIR flux, at 37 290 GM/c³ (Fig. 3). After the NIR flux peak, the NIR total flux stays elevated and reaches several lesser peaks over the course of roughly 1 hour before quickly returning to its median value.

This NIR flare is also accompanied by significant (\sim 2x) increases in both the sub-mm and mm $FWHM_{MIN}$ and $FWHM_{MAX}$. Both the sub-mm and mm size reach a peak value about 1 hour after the NIR total flux peak. The mm $FWHM_{MAX}$ peak lags behind the sub-mm $FWHM_{MAX}$ peak by 10 min. Near the peak value of the sub-mm and mm size increases, the NIR total flux curve quickly drops back to its median value. The sub-mm/mm sizes, however, slowly return to their quiescent values over the course of \sim 30 min.

Before the NIR flare, the sub-mm total flux shows significant variability between 2 Jy to 5 Jy. During the NIR flare, the sub-mm flux climbs again to 5 Jy. Therefore, the peak in sub-mm flux is not unique to periods with NIR flaring.

After the second 5 Jy peak, the sub-mm flux quickly drops below 2 Jy. The minimum in the sub-mm total flux curve is simultaneous with the sub-mm $FWHM_{MAX}$ peak as well as a minor peak in the NIR total flux curve (see dotted vertical blue line in Fig. 3).

The mm total flux, both during the quiescent and flaring periods, shows less variability than its sub-mm counterpart and stays near 2.5 Jy.

Fig. 3 also shows a minor NIR flare near 36 800 GM/c³, which is coincident with a minor magnetic flux eruption event. The NIR flux during the flare only reaches a peak value ~6 mJy and stays elevated for 80 min. Also, unlike the prominent NIR flare, there are no significant sub-mm/mm size increases within 1 h after the minor NIR flare. The low-density 'bubble' that forms during the minor flare is smaller in size than its counterpart from the prominent flare, demonstrating that the geometry of the bubble has an impact on the resulting sub-mm/mm size.

5 THE SUB-MM AND NIR CENTROID MOTION DURING A MAGNETIC FLUX ERUPTION

5.1 The NIR centroid

Prior to the prominent magnetic flux eruption discussed above from the high-spin, prograde simulation, the NIR centroid curves stay near the median value of (-6.5 μ as, 0.3 μ as). The NIR centroid position does not change significantly during the minor NIR flare (Fig. 3).

However, during the second, prominent NIR flare, the NIR centroid makes two orbits around the black hole over a period of \sim 3 h, tracing a quasi-circular path with a peak diameter of 46 μas (see the right side of Figs 4 and 3). The NIR centroid returns to its quiescent position at the end of the NIR flare.

5.2 Sub-mm centroid motion and linear polarization

During the prominent NIR example flare, the sub-mm centroid makes a similar, quasi-circular orbit on the sky as the NIR centroid over a

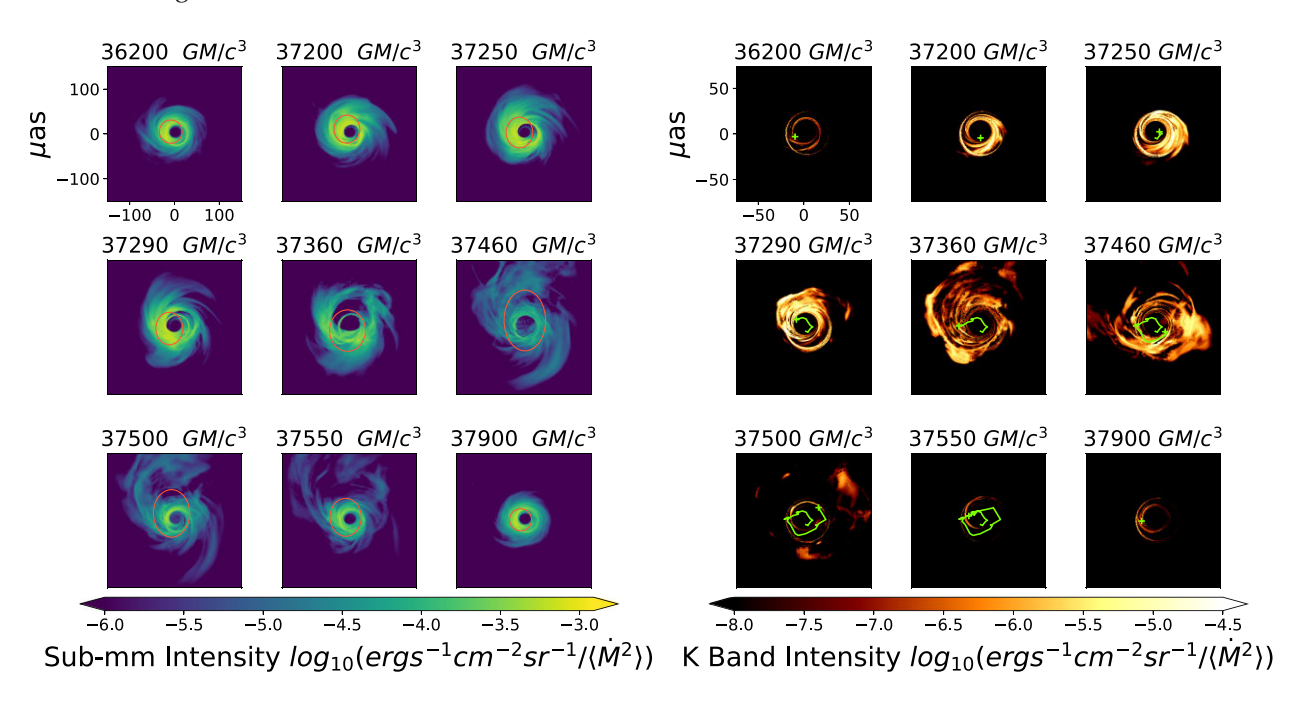


Figure 4. Select sub-mm (left panel) and NIR (right panel) images from the high-spin, prograde simulation that includes the example NIR flare. All times occur during the 2000 GM/c³ interval shown in Fig. 3. The NIR images are squares of $30 \, \text{GM/c}^2$ ($150 \, \mu$ as on the sky), the sub-mm images are squares of size $60 \, \text{GM/c}^2$ ($300 \, \mu$ as on the sky), and the black hole is centred at the origin in both sets of images. The minor and major axes of the red ellipse in the sub-mm correspond sub-mm $FWHM_{MIN}$ and $FWHM_{MAX}$, respectively. The green + in the NIR images is the NIR centroid position at the time of the image and past locations of the centroid are represented with a green line. First, a gap in the sub-mm intensity map forms that corresponds to the region of increased NIR emission. The NIR centroid also begins its first, counter-clockwise orbit (from $t = 37 \, 200 \, \text{to } 37 \, 290 \, \text{GM/c}^3$) around the black hole. At time $37 \, 360 \, \text{GM/c}^3$, the gap in the sub-mm intensity map is extremely pronounced and the sub-mm size continues to increase. The NIR intensity in the region $20-50 \, \mu$ as from the black hole centre also increases, pushing the NIR centroid further away from its median value and starting a second, larger orbit around the black hole. By $37 \, 460 \, \text{GM/c}^3$, when the sub-mm emission size is at a maximum, the gap in the sub-mm emission has dissipated but the emission in the $50-100 \, \mu$ as has increased whereas the emission closer to the black hole centre has decreased. As the sub-mm size decreases to its median value during times $37 \, 500 \, \text{to } 37 \, 550 \, \text{GM/c}^3$, the sub-mm intensity near the centre of the black hole increases and the extra emission in the outer regions dissipates. The NIR total flux drops significant during this time, but the NIR centroid makes it back to its median value by $37 \, 550 \, \text{GM/c}^3$. By $37 \, 900 \, \text{GM/c}^3$, both the sub-mm size and NIR centroid have returned to their median values.

period of ~ 3 h (Fig. 5). The sub-mm centroid position is also less noisy than its NIR counterpart. Considering both centroids follow the counter-clockwise motion of the accretion flow, the sub-mm centroid is ahead of the NIR centroid by ~ 20 min. The effective diameter of the sub-mm centroid path, which reaches an extreme at $28~\mu as$, is also smaller than its NIR counterpart.

During the 5 h prior to the flare, we find that the sub-mm linear polarization integrated over the image behaves like a random walk in Stokes \mathcal{U} and \mathcal{Q} space with an average linear polarization fraction $(p=(|\mathcal{U}|^2+|\mathcal{Q}|^2)/|\mathcal{I}|^2)$ of 4.5 per cent. However, right as the sub-mm centroid begins its quasi-circular path, the sub-mm polarization vector changes behaviour and slowly rotates in Stokes \mathcal{U} and \mathcal{Q} . For the first \sim 2 h, shown in Fig. 6, the path traced in Stokes \mathcal{U} and \mathcal{Q} space is a clear loop; the shape of the path in Stokes \mathcal{U} and \mathcal{Q} looses this character for the final \sim 1 h of the sub-mm centroid motion. While the polarization vector angle slowly rotates, the total linear polarization fraction reaches a maximum value of 11 per cent.

6 THE LUMINOSITY SPECTRUM AND SUB-MM SPECTRAL INDEX DURING A MAGNETIC FLUX ERUPTION

We calculate the spectrum ν $L(\nu)$ directly from the intensity maps by finding the total flux F_{ν} over a wide range of frequencies ν . Then, we find $L_{\nu}=4\pi D^2 F_{\nu}$, where D is the distance from the Galactic Centre to the observer.

The spectral index is defined as $\alpha \equiv -d\log{(F(\nu))}/d\log{\nu}$. We calculate the spectral index near 230 GHz (1.3 mm), $\alpha_{\rm submm}$, by finding $\log{(F(\log{(\nu))})}$ for five frequencies between 210 and 250 GHz and then fitting the function to a line using numpy.polyfit.

Fig. 7 shows the resulting spectra. The spectrum at $t=36\,200\,\mathrm{GM/c^3}$, when the accretion flow is an a quiescent state, has a shape similar to the power spectrum of a single electron and $\alpha_{\mathrm{submm}}=-0.07$. At the NIR flare peak ($t=37\,290\,\mathrm{GM/c^3}$), the high-frequency tail of ν $L(\nu)$ is significantly elevated with only a slight increase in luminosity for sub-millimeter and millimeter frequencies but α_{submm} remains relatively unchanged with a value of 0.06. There is also little to no change in the total luminosity for millimeter and radio frequencies.

When the simulated images of the accretion flow undergo sub-mm and mm size increases, the luminosity spectrum continues to evolve. At $(t = 37\,460\,\mathrm{GM/c^3})$, when the sub-mm size reaches its peak value, the spectrum becomes a combination of an elevated high-frequency tail and a synchrotron spectrum with a lower peak frequency ν_c than at the earlier, quiescent time. The shift in the peak synchrotron frequency is clearer at time $t = 37\,510\,\mathrm{GM/c^3}$, when the sub-mm size is still 1.6x times the median value but the NIR flare has dimmed.

This shift in the synchrotron thermal spectrum at $t=37\,460$ and $37\,510\,\text{GM/c}^3$ causes α_{submm} to become negative compared to the quiescent and peak NIR total flux times. We calculate $\alpha_{\text{submm}}=-0.84$ at the peak sub-mm size and $\alpha_{\text{submm}}=-0.49$ at $t=37\,510\,\text{GM/c}^3$.

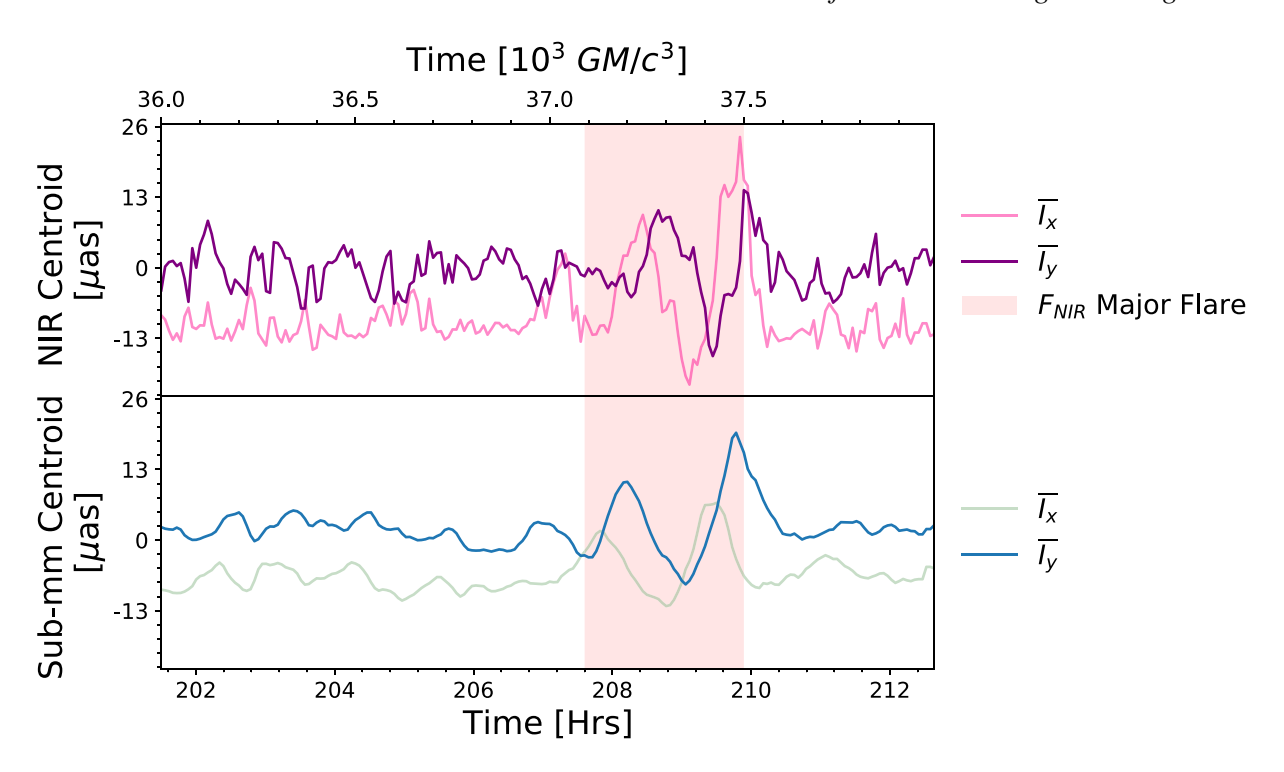


Figure 5. NIR and sub-mm centroid motion from the 2000 GM/c³ example which includes the prominent NIR flare, quiescent periods, and a minor flare. Both centroids stay close to their median values during quiescent periods and the first (minor) flare. However, during the second, more prominent flare, both the sub-mm and NIR centroids exhibit similar quasi-circular motion. The NIR centroid lags behind its sub-mm counterpart by \sim 20 min.

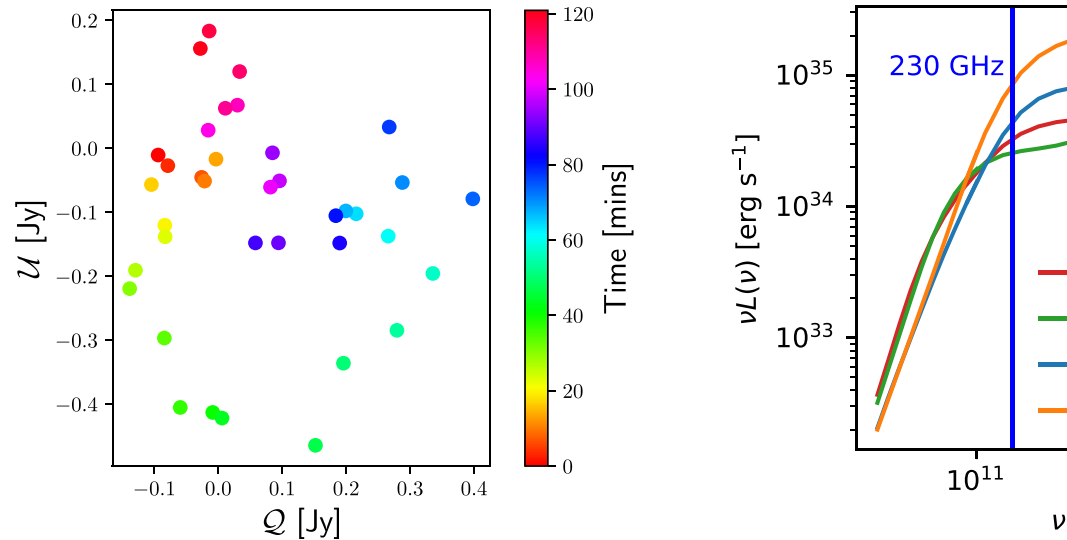


Figure 6. Integrated Stokes Q, \mathcal{U} for each time step during the example NIR flare explored in Section 4 and shown in Figs 3-5. The linear polarization slowly rotates in Stokes $\mathcal U$ and $\mathcal Q$ space over a period of 2h in a quasicircular pattern. In this example, polarization angle rotation is consistent with quasi-circular centroid motion at the same frequency on the sky.

7 BEHAVIOUR OF OBSERVABLES ACROSS ALL SIMULATIONS

7.1 NIR total flux and sub-mm size

By running the high-spin, prograde simulation to 96 310 GM/c³, we were able to characterize the long-term behaviour of the sub-mm and NIR total flux, centroid motion, and size. The autocorrelation

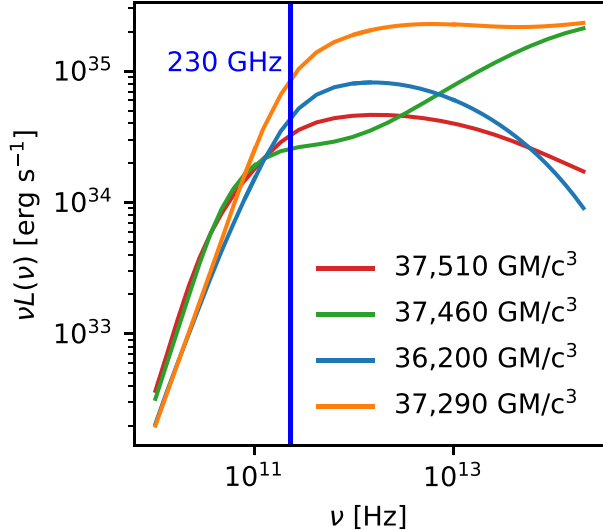


Figure 7. Luminosity spectra for the high-spin, prograde simulation at key times before, during, and after the example NIR flare. At $t = 36200 \,\text{GM/c}^3$, the accretion flow emission is in quiescence. The spectrum is flat at low frequencies and falls exponentially at high frequencies. During the peak value of the NIR total flux flare ($t = 37290 \,\mathrm{GM/c^3}$), the spectrum develops an elevated high-frequency tail but is only slightly elevated at sub-mm and mm frequencies; α_{submm} remains near zero. However, during the peak submm size, $\alpha_{\text{submm}} = -0.84$. A time steps later, at 37 510 GM/c³, the NIR flux is no longer elevated but the size is sill 1.6x the median value and α_{submm} remains negative. The sub-mm size increase is coincident with a shift in the synchrotron spectrum to lower frequencies and a more negative spectral index near 230 GHz.

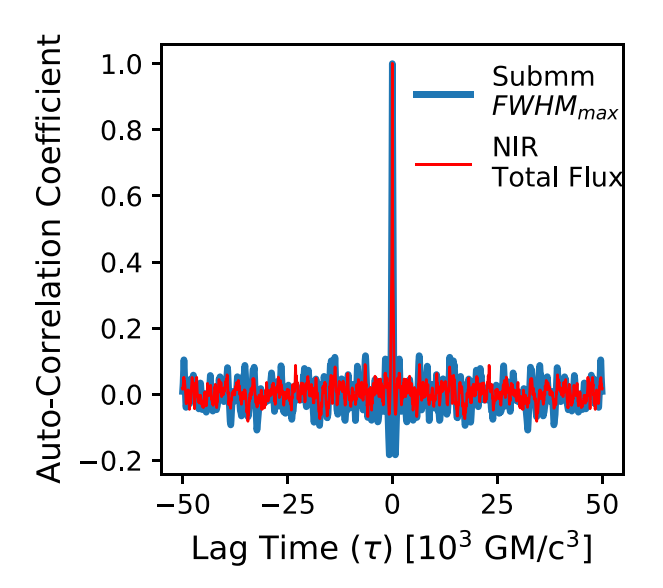


Figure 8. The autocorrelation functions for the NIR total flux (red) and the sub-mm maximum size increase (light blue) over the time 10 000 to $96\,310\,\text{GM/c}^3$ for the fiducial high-spin, prograde simulation. Besides the expected peak at $\tau=0$, there is no significant secondary peak for a τ range of from 0 to $50\,000\,\text{GM/c}^3$, just over half the simulation time. Therefore, there are no significant periods of recurrence for both the NIR total flux and the sub-mm size increases.

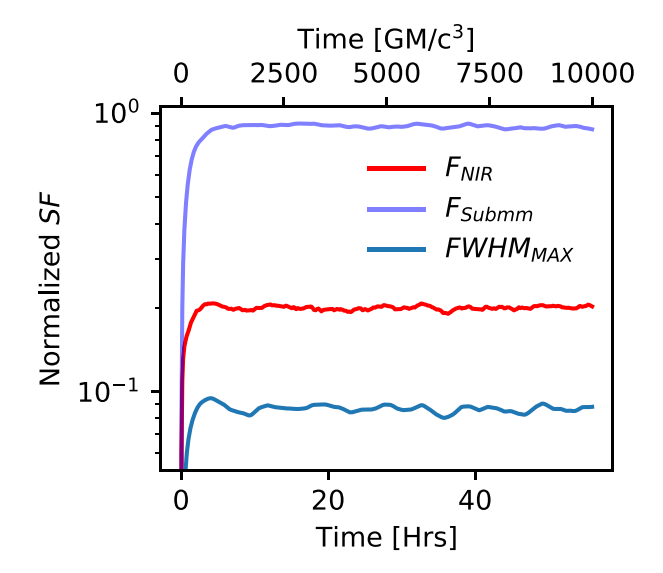


Figure 9. The structure function (SF, equation 9) for the total NIR flux F_{NIR} , total sub-mm flux F_{submm} , and the sub-mm max size increase $FWHM_{MAX}$ plotted a log scale for the fiducial high-spin, prograde simulation. Each curve is normalized by its mean value. The SF for F_{NIR} and F_{submm} reach a plateau value at \sim 5 h. The SF for the sub-mm $FWHM_{MAX}$ shows some variation over after reaching a peak value but still stays near the mean, normalized value of 0.18.

functions for both the NIR total flux and the sub-mm $FHWM_{MAX}$ (Fig. 8) show no prominent peaks besides $\tau=0$, demonstrating a lack of periodicity. The SFs SF for the NIR total flux, sub-mm total flux, and the sub-mm $FWHM_{MAX}$ (Fig. 9) all reach an asymptotic value τ_{SF} near 1000 GM/c³ (5 h for Sgr A*). Since the NIR total flux curve τ_{SF} is less than the time between magnetic flux eruptions, the NIR flares are likely independent from one another.

Significant increases in the sub-mm $FWHM_{MAX}$ follow many NIR flares during the high-spin, prograde simulation run (Fig. 10). This relationship, however, is not unique to our fiducial simulation and persists across our entire parameter space. Fig. 11 shows a positive example of a sub-mm size increase following an NIR flare for every simulation studied. The cross-correlation coefficient between the NIR total flux and the sub-mm $FWHM_{MAX}$ for every simulation has a single, significant peak with a value near 0.6, a positive characteristic time delay $\tau^* < 1$ h, and peak width of ~ 3 h (Fig. 13). In our convention, a positive τ^* means that the NIR total flux curve's behaviour precedes the sub-mm $FWHM_{MAX}$ curve's behaviour.

However, we do find a dependence between the black hole spin and accretion flow orientation on τ^* : low-spin and low initial tilt angle (θ_0) simulations produce the shortest $\tau^* \sim 20$ min while increasing either the spin or θ_0 increases the value of τ^* to 40–50 min.

In all simulations studied, the NIR total flux, unlike the sub-mm $FWHM_{\rm MAX}$, is intrinsically noisy. This noise reduces the value of the peak cross-correlation coefficient between the NIR total flux and the sub-mm $FWHM_{\rm MAX}$. Performing a moving average of only the NIR total flux for the high-spin, prograde simulation with a window size between 120–240 GM/c³ (40–80 min) preserves the periods of significant flaring while reducing the NIR total flux noise. When we correlate this averaged NIR total flux curve with the sub-mm $FWHM_{\rm MAX}$, the peak cross-correlation coefficient between the two curves increases from 0.6 to 0.7–0.8.

7.2 The probability of a sub-mm size increase

Although the cross-correlation coefficient illustrates the relationship between the NIR total flux and the sub-mm size increases, the curve alone does not assign a probability of a size increase given an NIR total flux flare. To derive those probabilities, we first define an *observation window* to be a time-ordered set of all observables within a fixed time interval. Each observation window is indexed by its start time. We define the random variable X as a Boolean-valued outcome of the following trial: a success is if there is at least one point within an observation window of the sub-mm $FWHM_{\rm MAX}$ above some threshold value $\alpha_{\rm FWHM}$, where $\alpha_{\rm FWHM}$ is normalized by the median sub-mm $FWHM_{\rm MAX}$, and a failure otherwise. We then define $f_{\rm NIR}$ as the total NIR flux normalized by its median value ($f_{\rm NIR} = F_{\rm NIR}/m(F_{\rm NIR})$). The Boolean random variable Y is then defined to be true if the total flux during an observation window ever exceeds the threshold value $f_{\rm NIR}$ and false otherwise.

We treat both X and Y random variables as independent and identically distributed. We then calculate the conditional probability $P(\alpha_{\text{FWHM}} > X | f_{\text{NIR}} > Y)$ for two fixed duration observation windows: 50 and 100 min.

Fig. 12 shows these conditional probabilities for the fiducial high-spin, prograde simulation. An increase in NIR flux during an observation window greatly improves chances of detecting a sub-mm size increase during the same window. Even restricting observations to periods of minor (x2 the median value) elevated NIR total flux significantly increases the chances of a positive sub-mm size increase detection. For NIR flares that reach 8x the median NIR total flux, the chance of detecting at least a moderate size increase > 90 per cent. Without considering the NIR total flux, the chance of detecting a moderate size increase is ~ 20 per cent.

7.3 The sub-mm and NIR flux

Unlike the consistent behaviour of the cross-correlation coefficients between the sub-mm size and the NIR total flux, the cross-correlation

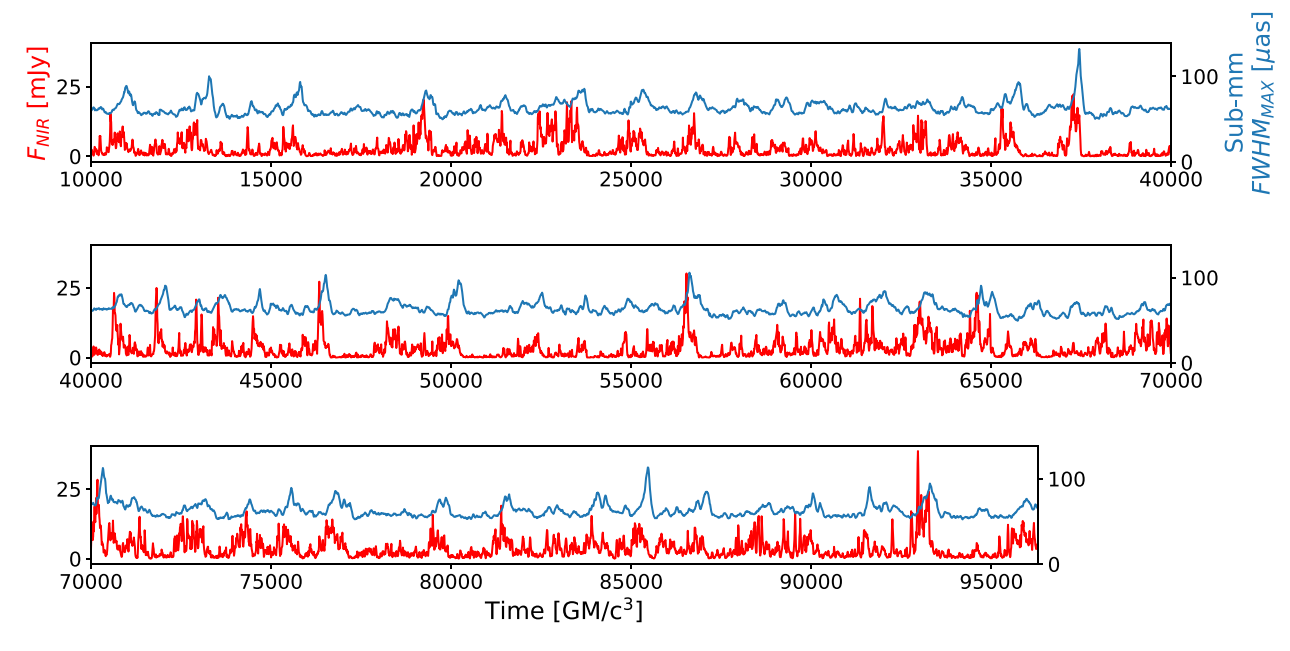


Figure 10. The Total NIR Flux and sub-mm $FWHM_{MAX}$ for the full (10 000 to 96 310 GM/c³) high spin, prograde simulation. Even at late times, there are many examples of significant size increases following a period of NIR flares. Some smaller amplitude flares are able to produce large size increases while large amplitude flares can produce less extreme size increases. As explored in the Discussion, the actual size increase observed is dependent on the geometry of the low-density, high-temperature bubble. The size increases generally have a single peak with similar rising and falling behaviour that corresponds to the ejection and then re-accumulation of material near the horizon, respectively. However, the NIR flares demonstrate a variety of morphologies. Some flares exhibit a single, extreme peak followed by lesser peaks (e.g. times \sim 57 000 and \sim 92 500 GM/c³) while other flares show several medium amplitude peaks in a row (near 23 000 and 89 000 GM/c³).

coefficient between the sub-mm total flux and NIR total flux varies significantly across the simulation parameter space (see Fig. 13, right panel). The resulting curves show a variety of peak values and values of the characteristic time τ^* . The peak of the cross-correlation coefficients are all near or significantly less than 0.5 and are also wider than their counterparts between the sub-mm size and the NIR total flux. Although we do find correlations between the sub-mm total flux and NIR total flux, the correlations between the sub-mm size and the NIR total flux is both stronger and more consistent than the former across our parameter space.

7.4 The NIR centroids

The NIR centroid motion varies considerably between flaring states and quiescent states. During quiescent periods, the NIR centroid stays near a median value with several 'jumps' around the black hole. However, during flaring periods, the NIR intensity map is dominated by a bright region which moves in a smooth, continuous motion. For some extreme NIR flares, this continuous motion forms a quasicircular pattern on the sky.

This qualitative behaviour occurs in all simulations studied. However, the effective diameter of the centroid path during different NIR flares varies considerably both during the course of a single simulation and across the simulation parameter space. The example from the fiducial simulation explored in Section 4 shows the largest (46 μ as) effective diameter an NIR centroid makes on the sky out of all simulations studied here. Other quasi-circular centroid motions during NIR flares from the same simulation show smaller effective diameters of \sim 25 μ as and periods of 80–120 min. With the exception of the a=0.3, $\theta_0=16^\circ$ simulation, which only produces centroid motion with a diameter of 17 μ as, the largest centroid motion diameters from other simulations explored range from \sim 20–25 μ as.

In the example from our fiducial simulation, the sub-mm centroid also traces a quasi-circular orbit on the sky while the NIR centroid makes a similar orbit. However, we find many examples of NIR flares across our parameter space that exhibit the quasi-circular NIR centroid motion without similar sub-mm centroid motion. However, these same NIR flare examples do display significant sub-mm size increases.

One interesting 9-h period of time during the prograde a = -0.5 simulation contains 10 consecutive NIR flares. During this period, the NIR centroid makes several loops around the sky rather than the usual one or two loops.

We can also use the cross-correlation coefficient to show that the quasi-circular motion NIR centroid seen during NIR flares does not continue during quiescent periods. We treat the x and y centroid components, \bar{I}_x and \bar{I}_y , as separate curves and find the cross-correlation coefficient between them, $\mathcal{CC}[\bar{I}_x,\bar{I}_y]$ for short $\sim 2000 \, \text{GM/c}^3$ (11 h) time intervals that contain a significant NIR flare and for the entire duration of the simulation. If the centroid traced a perfect ellipse on the sky with frequency ω , then the maximum of the cross-correlation coefficient $\mathcal{CC}[\bar{I}_x,\bar{I}_y]_{\text{MAX}}=1$ at $\tau=\sqrt{2}/2\omega$. For the short intervals of time, we find examples that reach $\mathcal{CC}[\bar{I}_x,\bar{I}_y]_{\text{MAX}}$ of 0.6–0.8. However, the values of $\mathcal{CC}[\bar{I}_x,\bar{I}_y]_{\text{MAX}}$ for the full duration of each simulation in our parameter space is much lower at 0.2–0.4. The upper-end of this interval comes from the a=-0.5 simulation where there is a 9 h period of NIR flaring that results in many orbits of the NIR centroid around the black hole.

8 DISCUSSION

In this work, we show that magnetic flux eruptions cause a lowdensity, high-temperature magnetized bubble to form in the inner accretion flow. This bubble orbits around the black hole and breaks

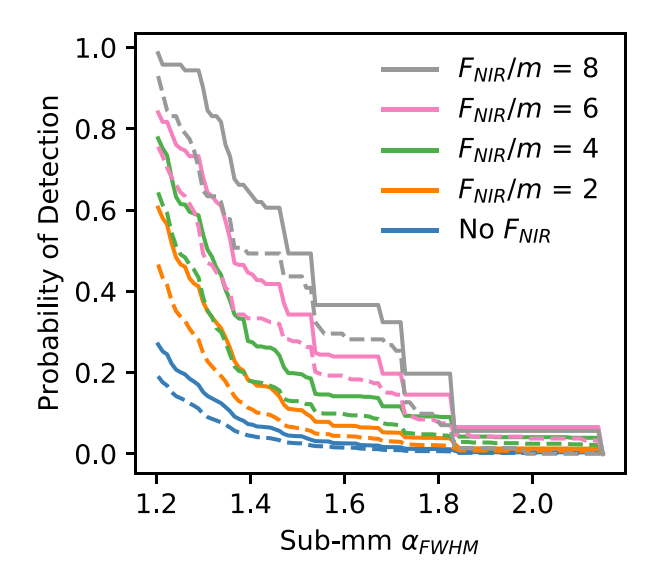


Figure 12. The probability of detecting at least one point in the fiducial highspin, prograde simulation where the normalized sub-mm FWHM_{MAX} is above some threshold α_{submm} given that the NIR total flux is also elevated above the normalized flux f_{NIR} at some point during the same time interval (observation window). We define the sub-mm $\alpha_{FWHM} = FWHM_{MAX}/m(FWHM_{MAX}) =$ $FWHM_{MAX}/61.5\mu$ as, where $m(FWHM_{MAX})$ is the median value of the submm $FWHM_{MAX}$ curve. The quantity $f_{NIR} = F_{NIR}/m(F_{NIR})$ and the median value of the NIR total flux is $m(F_{NIR}) = 2.2 \,\text{mJy}$. The solid lines correspond to a long, 100-min observation window and the dashed lines correspond to the short, 50 min-observation window. The blue lines correspond to $P(\alpha_{\text{FWHM}})$ > X) and the other lines correspond to $P(\alpha > X|F_{NIR}/m > N)$ for an integer N. Even restricting observations to periods of minor (x2) elevated NIR total flux significantly increases the chances of a positive sub-mm size increase detection. The stronger the flare, the higher the chance of detection. It is possible for the probability of a sub-mm size increase to reach 95 per cent if it occurred within an observation window containing an NIR flare that increased by a factor of x8 from its median value (such flares have already been observed, see Witzel et al. 2018; Do et al. 2019; GRAVITY Collaboration et al. 2020b).

into smaller regions before reaching large (> $30r_g$) radii. The low density of the bubble as well as temperature increases in the $\sigma < 1$ regions of the accretion flow lead to significant (1.5x-2x) increases in the sub-mm and mm emission region. These size increases follow NIR flares by ~ 1 h for the high-spin, prograde simulation. The mm size increase trails behind the sub-mm size increase by a few minutes, likely due to the fact that the mm emission region extends to larger radii compared to the sub-mm emission region. The sub-mm size increase coincides with a sudden drop in the sub-mm total flux and can cause the sub-mm spectral index to become more negative. This relationship between NIR flaring and sub-mm/mm size increases occurs over a parameter space of black hole spin and initial tilt angle: parameters currently unconstrained for Sgr A*.

We showed that magnetic flux eruptions produce quasi-circular centroid tracks for simulations over a variety of black hole spin values; the largest diameter track occurred during the high spin case. We identified several examples of NIR flares where the NIR centroid follows a quasi-circular path but the sub-mm centroid does not. The sub-mm and NIR centroid motions are weighed by nearly complimentary regions in their respective emission maps (see Fig. 4). There are also many sources that can effect the position of the sub-

mm centroid: the location of the shadow caused by the low-density 'bubble', additional heating outside the 'bubble', and the anisotropic geometry of the accretion flow itself. Therefore, NIR centroid motion does not guarantee similar sub-mm centroid motion.

We also considered a single, high spin (a=0.9375) SANE simulation with $\theta_0=16^\circ$. After running the simulation for 25 000 GM/c³, we found one example of a small NIR flare (<1 mJy) and no examples of significant sub-mm size increases. Therefore, the extreme variability in sub-mm size may be a unique feature of magnetic flux eruption events that occur in MAD simulations.

In our work, the accretion rate is fixed over $5000 \, \text{GM/c}^3$ periods of time by matching the calculated, average sub-mm total flux to its observed value ($\sim 3 \, \text{Jy}$) for Sgr A*. In the real Sgr A* system, stellar winds from the $\sim 30 \, \text{Wolf-Rayet}$ stars that populate the Galactic Centre provide a significant source of accretion material (Ressler, Quataert & Stone 2018, 2019; Ressler et al. 2020).

8.1 Electron heating, non-thermal electrons, and σ -cut

Self-consistently evolving the electron temperature requires a choice of electron heating prescription.

In their study of sub-mm emission from a magnetic flux eruption, Jia et al. (2023) applied the $R_{\rm high}-R_{\rm low}$ electron heating model (Mościbrodzka, Falcke & Shiokawa 2016), where $R\equiv T_{\rm p}/T_{\rm e}$. They demonstrated that, for high $T_{\rm e}$ models, setting $R=1,\,10$, and ray-tracing images with the $\sigma>1$ regions excluded produced a steady decline in the sub-mm total flux and did not produce significant sub-mm size increases. However, setting R=100 caused an increase in the sub-mm size. The sub-mm total flux also increased in the latter case before fading.

For this study, we chose the electron heating prescription W18 (Werner et al. 2018) because it was the most successful model in matching mm to NIR observations of Sgr A* (Dexter et al. 2020a) and producing NIR centroid motions. Models of PIC turbulent electron heating and heating during reconnection for an electron/ion plasma is still an active field of study. Future results in this field will provide new prescriptions and more accurate predictions of observables from our models. Here, we also apply the W18 electron heating fraction uniformly regardless of whether reconnection is occurring. Future studies could account for spatial variation in the heating mechanism, instead of solely the fluid magnetization.

In our model, the electrons in the accretion flow are thermal. Relativistic reconnection (Sironi & Spitkovsky 2014; French et al. 2023; Hakobyan, Ripperda & Philippov 2023) the magnetic Rayleigh—Taylor instability (Zhdankin et al. 2023) are possible sources for non-thermal particles in the accretion flow. Non-thermal particles can significantly increase the NIR total flux while having a less pronounced effect on the sub-mm/mm observables (Dodds-Eden et al. 2009; Scepi, Dexter & Begelman 2022). Non-thermal particles may also be the cause of the large mm size on the sky compared to what is calculated in this work. Non-thermal emission may also decrease the true NIR flux if electrons actually emit at higher frequencies (such as the X-ray).

In the images presented in our Results, we also excluded the high $\sigma>1$ regions of the accretion flow (σ -cut = 1). As shown in Fig. 1, large regions of the innermost accretion flow ($r\lesssim 10r_{\rm g}$) reach $\sigma>1$ values during a magnetic flux eruption. Setting σ -cut = 10 includes most of the highly magnetized bubble in the image while still excluding the jet.

Increasing σ -cut to 10 only produces a slight (2 μ as) increase in the sub-mm size during quiescence compared to its σ -cut = 1

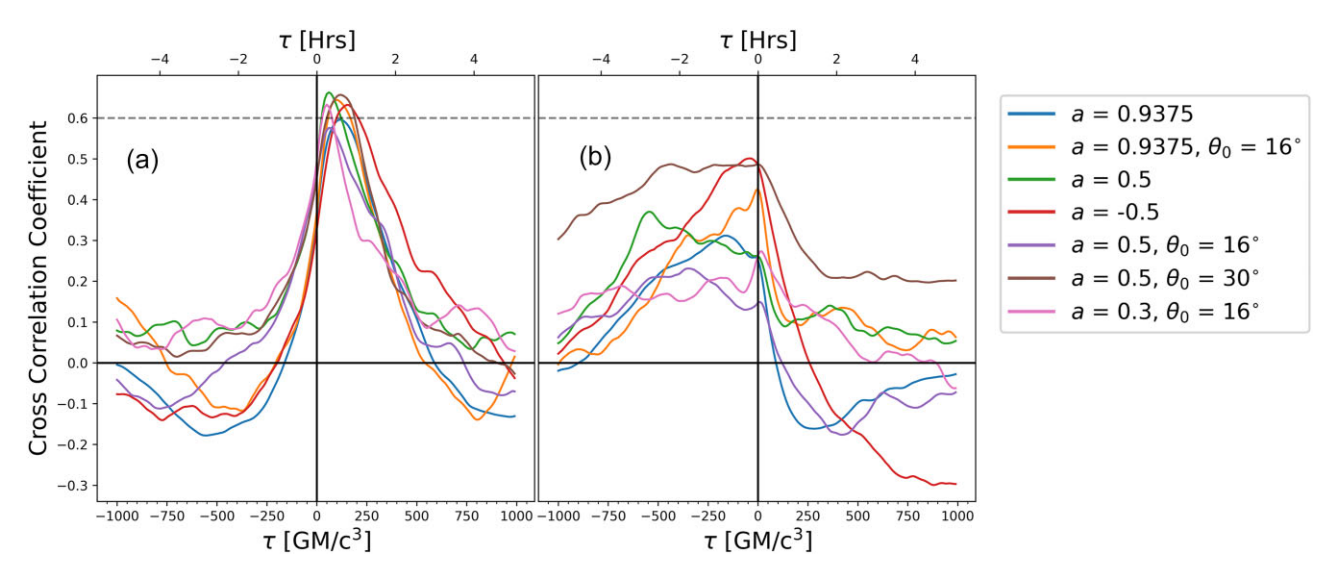


Figure 13. Panel a: the cross-correlation coefficient as a function of lag time τ between the NIR total flux and the sub-mm $FWHM_{MAX}$ for all simulations studied in this paper. The dotted grey line represents a cross-correlation coefficient value of 0.6. Regardless of initial tilt angle θ_0 or spin a, all simulations demonstrate a strong, singular cross-correlation coefficient peak of about 0.6 and a characteristic time delay τ^* between 20 and 60 min. Simulations with low spin and low initial tilt have shorter peak lag times than those with high spins or moderate to high initial tilt angles. Panel b: the cross-correlation coefficients between the NIR and the sub-mm total flux show both wider peaks and smaller peak values than their counterparts between the NIR total Flux and sub-mm $FWHM_{MAX}$. There is also greater variability of the cross-correlation peak values, the peak lag times, and the peak widths across our parameter space for the NIR and sub-mm total flux versus NIR total flux and sub-mm $FWHM_{MAX}$. Therefore, a correlation between the NIR and sub-mm total flux exists but is weaker and less consistent than the correlation between the NIR total flux and sub-mm $FWHM_{MAX}$.

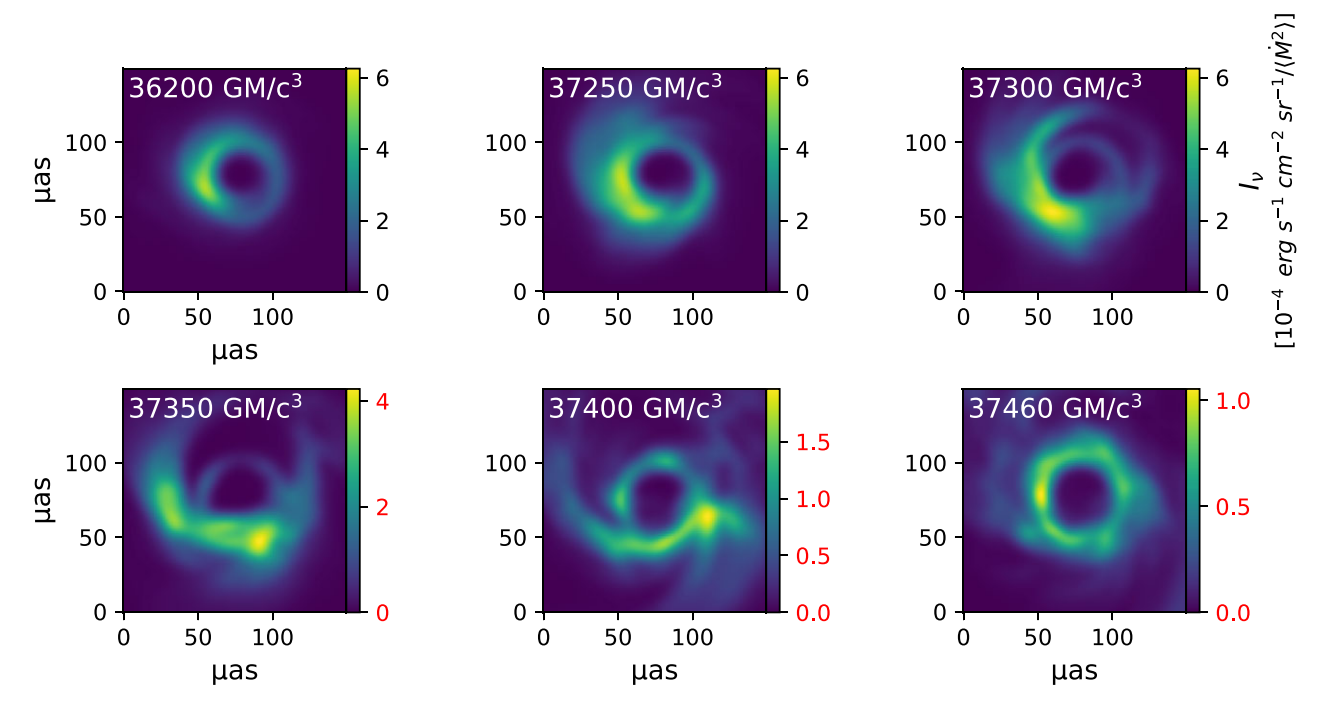


Figure 14. Simulated sub-mm (230 GHz) ground truth images using a 20- μ as FWHM Gaussian kernel for the fiducial NIR flare example shown in Figs 3 and 5. The field of view is 150μ as; note that the colour bar scale differs for the bottom row of images. The image intensity is plotted on a linear scale. The bright spot in the emission region clearly rotates around the black hole and the emission region also undergoes prominent morphological changes.

counterpart. The σ -cut = 10 images from our fiducial example still show a sub-mm size increase reaching 2x its median value. The gap that forms in sub-mm intensity maps also persist in the high σ image, demonstrating this gap is due to the drop in density in the region rather than an artificial omission of emission stemming from our choice of

a low σ cut. The difference in major axis of the peak sub-mm size between σ -cut = 10 and σ -cut = 1 is negligible ($< 0.002 \,\mu as$) while the minor axis only increases in the higher σ -cut case by $\sim 3 \,\mu as$. The σ -cut = 10 NIR images produce roughly double the total NIR flux compared their σ -cut = 1 counterparts (see Dexter et al. 2020b

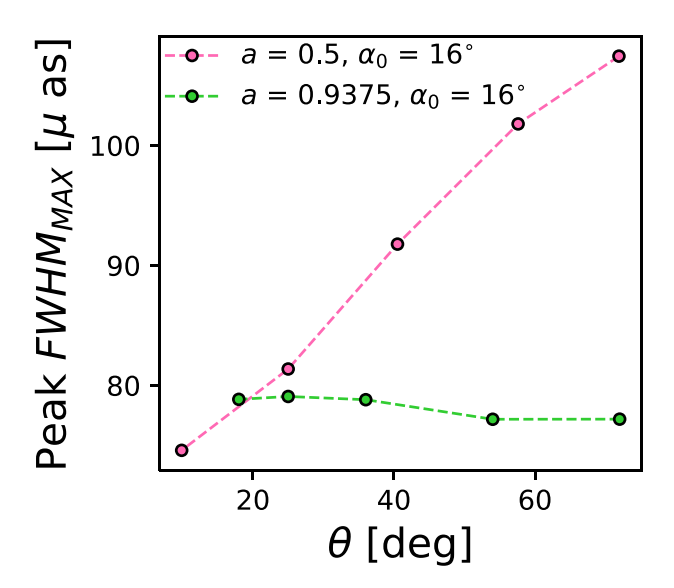


Figure 15. Two extremes of inclination angle dependence on the sub-mm (230 GHz) maximum size. Both curves show a size increase that occurred after a flaring event: The green line is taken from the a=0.9375, $\theta_0=16^\circ$ simulation and the pink line comes from the a=0.5, $\theta_0=16^\circ$ simulation. In the pink example, the peak value of the sub-mm maximum size curve grows linearly with angle. By contrast, in the green example, the size increase stays relatively flat for a variety of inclinations. In both examples, the peak size increase is significantly elevated from its median value for all inclination angles.

for further discussion on the choice of σ -cut and its effect on the NIR image.)

8.2 Electron cooling

Electrons radiating at a frequency ν lose energy and cool over a time-scale $t_{\rm syn} \propto \nu^{-1/2}$. We do not include synchrotron cooling in our simulations. Recent results suggest that radiative cooling can effect the total luminosity and flux peaks in both the millimeter and NIR wavelengths (Yoon et al. 2020). Non-thermal electrons in the accretion flow will also radiate at high energies and cool. PIC studies of electron/positron pair reconnection show that radiative models produce different power laws than their non-radiative counterparts (Werner, Philippov & Uzdensky 2019; Sironi & Beloborodov 2020).

For the NIR photons, $t_{\rm syn,NIR} \sim 10\,\rm min$. Because $t_{\rm syn,NIR}$ is less than both the flare time-scale and the duration of the quasi-circular NIR centroid orbits, cooling may have a significant impact on our results.

The sub-mm synchrotron cooling time, by contrast, is \sim 4 h and much longer than the time scale for the sub-mm size increases (\sim 2 h) and sub-mm centroid motion. Also, the sub-mm total flux value is manually fixed. However, the sub-mm size increases are highly dependent on the hot, low-density bubble from forming in the first place. If the hot NIR electrons cool too quickly in the real accretion flow, the bubble may dissipate more rapidly and not lead to such large sub-mm size increases.

8.3 MAD GRMHD models and simulation resolution

Our models are subject to the same numerical computation constraints found in other magnetically dominated GRMHD simulations.

Strongly magnetic regions are difficult to evolve but are present in the low-density 'bubble' that drives size increases and centroid motion.

Extreme resolution ($5376 \times 2304 \times 2304$) GRMHD simulations of black hole accretion flows produce magnetic flux eruption events that show reconnection features such as plasmoids and X-points (Ripperda et al. 2022). However, the extreme resolution simulations produced lower reconnection rates than its lower resolution counterpart because of the larger numerical resistivity in the latter case (Ripperda et al. 2022). Still, magnetic reconnection in GRMHD simulations is generally slower than in PIC (kinetic) simulations because of pressure anisotropies that are not well captured in MHD (Bessho & Bhattacharjee 2005; Bransgrove, Ripperda & Philippov 2021). Therefore, the duration of the magnetic flux eruption events in this work may be overestimated or underestimated.

Numerical diffusivity likely effects the boundary of the highly magnetized bubble as it orbits around and away from the black hole. The temperature increases directly outside the $\sigma>1$ region leads to changes in the sub-mm size and NIR total flux. Studying changes in sub-mm and NIR images from higher resolution GRMHD simulations may demonstrate if the sub-mm size increases (and their relationship to the NIR total flux shown in this work) depend strongly on our choice of resolution. At lower resolution (1/2 to 3/4 the number of cells compared to the resolution explored here), Dexter et al. (2020b) found that NIR hot spot formation and rotation around the black hole still occurs.

Despite the success of MAD accretion flows in explaining a variety of Sgr A* observations, there still exists some tension between simulated observables and real observations. Event Horizon Telescope Collaboration et al. (2022c) concluded that, although MAD models with inclination angles <30° were preferred, no model in their library of static images met all their observational constraints.

8.4 Dynamic imaging with the EHT

EHT imaging algorithms are sensitive to ring morphologies (Event Horizon Telescope Collaboration et al. 2022b). In order to recreate the resolution of the constructed EHT image from interferometric data, we blur the $150 \times 150 \, \mu as^2$ region centred on the black hole in our sub-mm simulated images with a 20- μas FWHM Gaussian kernel. We focus on the blurred sub-mm before and during the fiducial NIR flare (Fig. 14). Not only do we find that the resulting structure is ring-like in all images, but we can clearly see the sub-mm hotspot rotating around the black hole centre. The effective shadow in the middle of the ring is also larger during a sub-mm size increase than during quiescence. Further analysis with dynamic imaging algorithms is required to confirm whether this variability can be reconstructed with current EHT or ngEHT u, v coverage.

8.5 Inclination angle and the sub-mm/mm peak size

Observations of Sgr A* are broadly consistent with a low inclination angle (GRAVITY Collaboration et al. 2018; Event Horizon Telescope Collaboration et al. 2022c) and motivate our choice of $i=25^{\circ}$. However, the exact value of the inclination angle to Sgr A* is still unclear. We varied the inclination angle for the time interval containing NIR flares from several simulations and studied the effect on the peak sub-mm size increase. The peak sub-mm size increase can remain prominent for very low (10°) and very high (73°) inclination angles. However, the exact relationship between the sub-mm peak value and the inclination angle can vary dramatically for different NIR flare examples. Fig. 15 demonstrates two extremes of this relationship. In one example, the sub-mm peak size is significantly

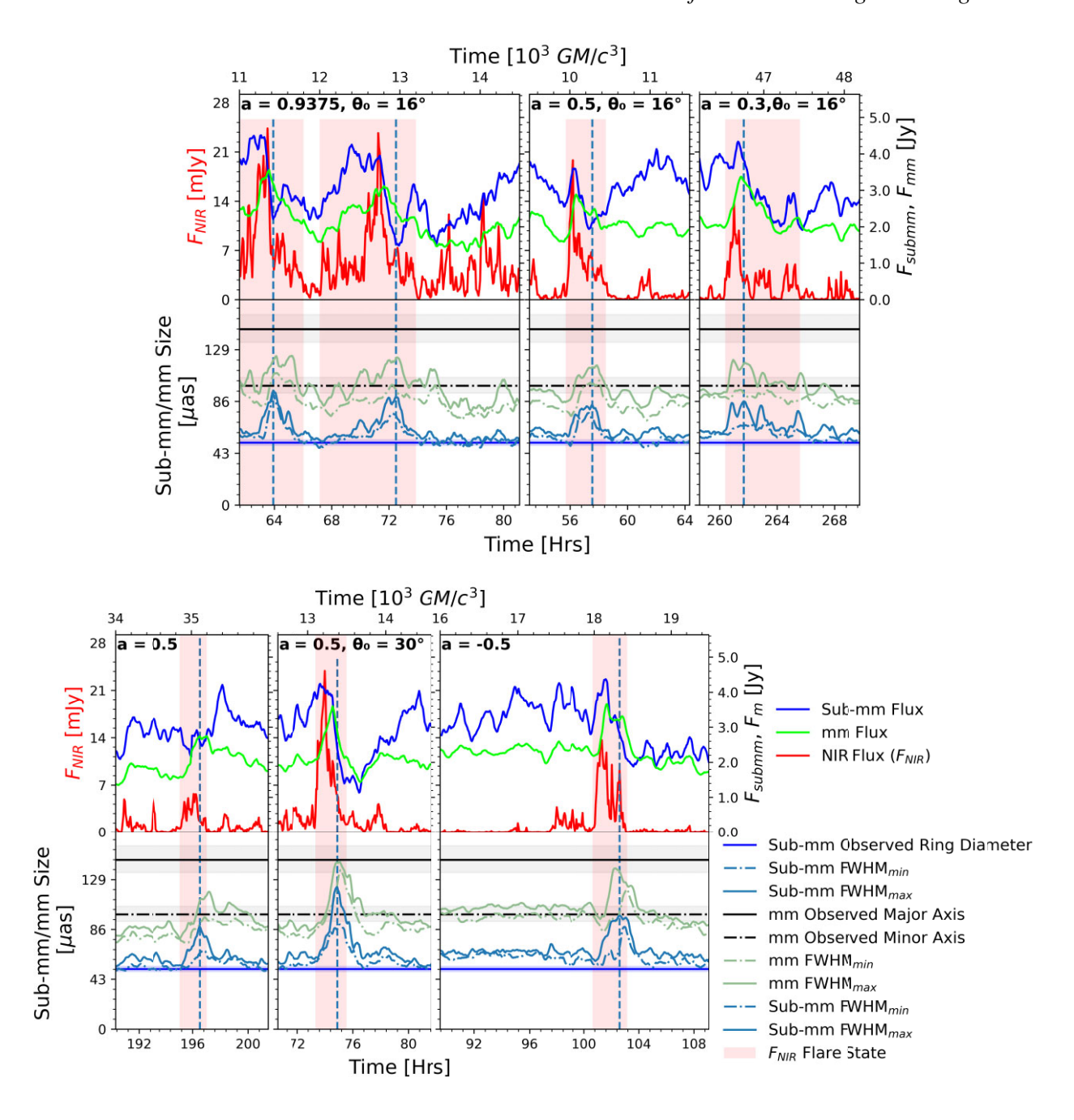


Figure 11. Examples of an NIR flare followed by a sub-mm and mm emission region size increase for every simulation studied in this work (with the exception of the fiducial simulation already shown in Fig. 3). Every column is a selected interval of time from a different simulation; the spin a and initial tilt angle θ_0 of the simulation are written in bold in each top left corner. The light red region highlights the interval of time where the NIR total flux is in a flare state. The light blue, dashed line aligns with the time where the sub-mm $FWHM_{MAX}$ is at a maximum. The black, horizontal solid and dashed lines are the observed median intrinsic (de-scattered) mm (86 GHz) major and minor axis, respectively, from Issaoun et al. (2021). The grey, shaded region corresponds to uncertainty (95 per cent confidence interval) of the mm observed size. The blue, horizontal line represents the observed sub-mm size and the light blue shaded region is the boundary of the 68 per cent confidence interval of the observed sub-mm size (Event Horizon Telescope Collaboration et al. 2022a). In all the examples shown, the sub-mm size increase peak occurs a few minutes before the mm size increase peak. All simulations produce the observed sub-mm size during quiescent periods, but both the mm size and eccentricity is lower than the observed value.

elevated from the median size value but remains flat as a function of inclination angle. In the second example, the sub-mm peak size grows roughly proportionally to the inclination angle.

Since $1.3 \, \text{mm}$ ($230 \, \text{GHz}$) is near the synchrotron spectrum peak, the intensity map at $1.3 \, \text{mm}$ is sensitive to the underlying density distribution of the gas. The actual shape of the low-density,

high-temperature region resulting from the magnetic flux eruption event varies considerably. Therefore, the shape of the 1.3-mm emission region will also vary. Although the examples come from two simulations with different spin a, it is unclear if a has an strong effect on this relationship between inclination angle and peak submm size.

8.6 Comparison to the observed 86/230-GHz quiescent size and observed NIR centroid

All simulations explored in this work reproduce the observed submm EHT size during quiescent periods, although the median sub-mm size can be slightly (\sim 15 per cent) larger than the observed sub-mm EHT size.

By contrast, there is tension between our modelled mm size and the observed mm size. Our simulations consistently produce a maximum quiescent mm size that is about 30 per cent lower than the observed value from the most recent analysis of ALMA data from 2017 April 3, (Issaoun et al. 2021). The quiescent eccentricity of the mm (86 GHz) emission is near zero in these simulations whereas the observed value is \sim 0.7. Interestingly, the predicted size and eccentricity matche the ALMA data well during a mm size increase following an NIR flare (see Fig. 3 from Section 4). Future observations may shed light on the true distribution of the mm size and its variability following NIR

The fiducial NIR flare studied here still produces an NIR centroid track diameter that is a factor of 3 smaller than observed diameter from the GRAVITY 2018 measurement (GRAVITY Collaboration et al. 2018). With an effective diameter of $46 \mu as$, the NIR centroid motion from the featured example is also the largest in our parameter space. NIR centroid motions with diameters of $\sim 15-25 \mu$ as are more common in our simulations but 7x - 8x smaller than the observed value. Sources of non-thermal NIR emission missing from our model, such as particle acceleration and synchotron cooling, can account for the discrepancy in the NIR orbit size (Ball et al. 2021).

9 CONCLUSIONS

GRMHD simulations of MADs undergo magnetic flux eruptions that power NIR flares and may explain the NIR centroid motion observed by GRAVITY. Additionally, the same class of simulations predict significant and frequent sub-mm and mm size increases that occur within a 2-h window after an NIR total flux peak. The models presented here make a clear, qualitative prediction within reach of the Next Generation Event Horizon Telescope.

ACKNOWLEDGEMENTS

The authors thank D. Uzdensky, A. Hankla, P. Dhang, and T. Mc-Maken for their helpful comments. This work was supported in part by NASA Astrophysics Theory Program grant 80NSSC20K0527, Fermi award 80NSSC21K2027, Chandra award TM3-24003X, and by an Alfred P. Sloan Research Fellowship.

DATA AVAILABILITY

Simulated images and averaged simulation data products used here will be shared on reasonable request to the corresponding author.

REFERENCES

Baganoff F. K. et al., 2001, Nature, 413, 45

Balbus S. A., Hawley J. F., 1998, in Holt S. S., Kallman T. R.eds, AIP Conf. Ser., Vol. 431, Accretion processes in Astrophysical Systems: Some like it hot! - eigth AstroPhysics Conference. Am. Inst. Phys., New York, NY. p. 79

Balick B., Brown R. L., 1974, ApJ, 194, 265 Ball D., Özel F., Christian P., Chan C.-K., Psaltis D., 2021, ApJ, 917, 8

Begelman M. C., Scepi N., Dexter J., 2022, MNRAS, 511, 2040 Bessho N., Bhattacharjee A., 2005, Phys. Rev. Lett., 95, 245001

Bisnovatyi-Kogan G. S., Ruzmaikin A. A., 1976, Ap&SS, 42, 401 Bransgrove A., Ripperda B., Philippov A., 2021, Phys. Rev. Lett., 127, 055101 Chan C.-k., Psaltis D., Özel F., Medeiros L., Marrone D., Sadowski A., Narayan R., 2015, ApJ, 812, 103 Chashkina A., Bromberg O., Levinson A., 2021, MNRAS, 508, 1241 Collaboration T. E. H. T. 2022, ApJ, 930, L12 Dexter J., 2016, MNRAS, 462, 115

Bisnovatyi-Kogan G. S., Ruzmaikin A. A., 1974, Ap&SS, 28, 45

Dexter J., Agol E., Fragile P. C., 2009, ApJ, 703, L142

Dexter J. et al., 2020a, MNRAS, 494, 4168

Dexter J. et al., 2020b, MNRAS, 497, 4999

Dexter J., Kelly B., Bower G. C., Marrone D. P., Stone J., Plambeck R., Doeleman S. S., 2022, ApJ, 930, L19

Do T. et al., 2019, ApJ, 882, L27

Dodds-Eden K. et al., 2009, ApJ, 698, 676

Dodds-Eden K. et al., 2011, ApJ, 728, 37

Eckart A. et al., 2008, A&A, 479, 625

Ekers R. D., Goss W. M., Schwarz U., Downes D., Rogstad D. H., 1975, A& A, 43, 159

Event Horizon Telescope Collaboration et al., 2022a, ApJ, 930, L12

Event Horizon Telescope Collaboration et al., 2022b, ApJ, 930, L14

Event Horizon Telescope Collaboration et al., 2022c, ApJ, 930, L16

French O., Guo F., Zhang Q., Uzdensky D. A., 2023, ApJ, 948, 19

Gammie C. F., McKinney J. C., Tóth G., 2003, ApJ, 589, 444

Genzel R., Eckhart A., Ott T., Eisenhauer F., 1997, MNRAS, 291, 219

Genzel R., Schödel R., Ott T., Eckart A., Alexander T., Lacombe F., Rouan D., Aschenbach B., 2003a, Nature, 425, 934

Genzel R., Schödel R., Ott T. abd Eckart A., Alexander T., Lacombe F., Rouan D., Aschenbach B., 2003b, Nature, 425, 934

Ghez A. M. et al., 2004, ApJ, 601, L159

Ghez A. et al., 2008, ApJ, 689, 1044

GRAVITY Collaboration et al., 2018, A&A, 618, L10

GRAVITY Collaboration et al., 2020a, A&A, 635, A143

GRAVITY Collaboration et al., 2020b, A&A, 638, A2

GRAVITY Collaboration et al., 2021, A&A, 654, A22

Hakobyan H., Ripperda B., Philippov A. A., 2023, ApJ, 943, L29

Hawley J. F., Balbus S. A., 1991, ApJ, 376, 223

Hughes P. A., Aller H. D., Aller M. F., 1992, ApJ, 396, 469

Igumenshchev I., Narayan R., Abramowicz M. A., 2003, ApJ, 592, 1042 Issaoun S. et al., 2021, ApJ, 915, 99

Jia H., Ripperda B., Quataert E., White C. J., Chatterjee K., Philippov A., Liska M., 2023, MNRAS

Lo K., Schilizzi R. T., Cohen M., Ross H., 1975, ApJ, 202, L63

MacLeod C. L. et al., 2010, ApJ, 721, 1014

Markoff S., Falcke H., Yuan F., Biermann P. L., 2001, A&A, 379, L13

Marrone D. P., Moran J. M., Zhao J.-H., Rao R., 2006, J. Phys. Conf. Ser.,

Mościbrodzka M., Falcke H., Shiokawa H., 2016, A&A, 586, A38

Narayan R., SÄ dowski A., Penna R. F., Kulkarni A. K., 2012, MNRAS, 426,

Noble S. C., Gammie C. F., McKinney J. C., Del Zanna L., 2006, ApJ, 641,

Ponti G. et al., 2017, MNRAS, 468, 2447

Ressler S. M., Tchekhovskoy A., Quataert E., Chandra M., Gammie C. F., 2015, MNRAS, 454, 1848

Ressler S. M., Quataert E., Stone J. M., 2018, MNRAS, 478, 3544

Ressler S. M., Quataert E., Stone J. M., 2019, MNRAS, 482, L123

Ressler S. M., White C. J., Quataert E., Stone J. M., 2020, ApJ, 896,

Ripperda B., Bacchini F., Philippov A. A., 2020, ApJ, 900, 100

Ripperda B., Liska M., Chatterjee K., Musoke G., Philippov A. A., Tchekhovskoy A., Younsi Z., 2022, ApJ, 924, L32

Scepi N., Dexter J., Begelman M. C., 2022, MNRAS, 511, 3536

Schodel R., Morris M., Muzic K., Alberdi A., Meyer L., ExkEckhart A., Gezari D. Y., 2011, A&A, 532, A83

Simonetti J. H., Cordes J. M., Heeschen D. S., 1985, ApJ, 296, 46

Sironi L., Beloborodov A. M., 2020, ApJ, 899, 52

Sironi L., Spitkovsky A., 2014, ApJ, 783, L21

Tchekhovskoy A., 2019, Astrophysics Source Code Library, record ascl:1912.014

Tchekhovskoy A., Narayan R., McKinney J. C., 2011, MNRAS, 418, L79

Trippe S., Paumard T., Ott T., Gillessen S., Eisenhauer F., Martins F., Genzel R., 2007, MNRAS, 375, 764

Werner G. R., Uzdensky D. A., Begelman M. C., Cerutti B., Nalewajko K., 2018, MNRAS, 473, 4840

Werner G. R., Philippov A. A., Uzdensky D. A., 2019, MNRAS, 482, 1.60

Wielgus M. et al., 2022, A&A, 665, L6

Witzel G., 2018, ApJ, 863, 15

Yoon D., Chatterjee K., Markoff S. B., van Eijnatten D., Younsi Z., Liska M., Tchekhovskoy A., 2020, MNRAS, 499, 3178

Zhdankin V., Ripperda B., Philippov A. A., 2023, Phys. Rev. Res., 5, 043023

This paper has been typeset from a T_EX/IAT_EX file prepared by the author.